CONTRACTION/EXPANSION EFFECTS IN 90° MITER BENDS IN RECTANGULAR XUROGRAPHIC MICROCHANNELS

by

Lam Trung Nguyen

A thesis submitted to the faculty of
The University of Utah
in partial fulfillment of the requirements for the degree of

Master of Science

Department of Mechanical Engineering

The University of Utah

August 2011

The University of Utah Graduate School

STATEMENT OF THESIS APPROVAL

The thesis of **Lam Trung Nguyen**

has been approved by the following supervisory committee members:

Timothy A. Ameel	, Chair	**05/04/2011** Date Approved
Bruce K. Gale	, Member	**05/04/2011** Date Approved
Meredith M. Metzger	, Member	**05/04/2011** Date Approved

and by **Timothy A. Ameel** , Chair of the Department of **Mechanical Engineering**

and by Charles A. Wight, Dean of The Graduate School.

ABSTRACT

Xurography is an inexpensive rapid prototyping technology for the development of microfluidic systems. Imprecision in the xurographic tape cutting process can result in undesired changes in channel dimensions near features that require a change in cutting direction, such as 90° miter bends. An experimental study of water flow in rectangular xurographic microchannels incorporating 90° miter bends with different channel widths in each leg is reported. A set of 12 microchannels, with channel depth approximately 105 micrometers and aspect ratio ranging from 0.071 to 0.435, were fabricated from double-sided adhesive Kapton® polyimide tape and two rectangular glass plates. The channels were reinforced with a mechanical clamping system, enabling high Reynolds number *Re* flows (up to $Re = 3200$) where *Re* was based upon hydraulic diameter and average velocity. Reported data include friction factor and critical Reynolds number for straight microchannels and loss coefficients for flow through 90° miter bends that contain either a contraction or expansion with cross-sectional area ratios of 0.5, 0.333 and 0.2. The critical Reynolds number, Re_{cr}, ranged from 1700 to 2300 and was found to be dependent on channel defects such as sidewall roughness, adhesive droplets, and corner imperfections. Loss coefficients through 90° miter bends with expansion decrease rapidly for $Re < Re_{cr}$. At the transition, the loss coefficient suddenly drops and approaches an asymptotic value for $Re > Re_{cr}$. For 90° miter bends with contractions, loss coefficients gradually decrease with increasing *Re* for $150 < Re < 1400$. In addition, the loss

coefficient decreases with decreasing area ratio through the contraction or expansion. The minor loss coefficient data were found to be dependent on Reynolds numbers and area ratio of contraction/expansion at the bend. The results suggest that the effect of the contraction/expansion was the dominant mechanism for minor losses in the 90° miter bend.

To my parents,

Hoa and Hieu Nguyen

CONTENTS

LIST OF FIGURES

LIST OF TABLES

ACKNOWLEDGEMENTS

This study would not have been possible without the guidance and the help of several individuals who in one way or another contributed and extended their valuable assistance in the preparation and completion of this study. First and foremost, I would like to express my sincere gratitude to my adviser, Dr. Timothy Ameel, for his continuous support, his patience, motivation and immense knowledge. Without his advisement, encouragement and valuable instruction, it would have been impossible for me to finish this study. I wish to thank Rahul Kolekar and Daniel Torgerson for their suggestions and assistance to the work in this study. The knowledge gained from their previous studies definitely saved countless hours. The suggestion and constructive comments from Dr. John Elsnab were valuable. I am grateful to Dr. Bruce Gale for the access to the cutting plotter in his laboratory. A special thank to Dr. Gernot Laicher from the University of Utah Physics Department for his assistance in setting up the laser interferometry system and access to his equipment. I also owe a special thank to Dr. Brian Devener for his assistance on using the Zygo optical profilometer. Last but not least, I would like to thank my family for their spiritual support throughout this study.

CHAPTER 1

INTRODUCTION

1.1 Motivation

Microelectromechanical systems (MEMS) have had a significant impact in medicine and bioengineering, information technology and many other industries for the last two decades [1]. Due to this rapid development of new fields in MEMS and microfluidics, many researchers and designers have taken a greater interest in fluid flow in microchannels. Many microfluidic devices require the use of microchannels and chambers. In addition to connecting different devices, microchannels are used for drug delivery systems, physical particle separation, and inkjet print heads and heat exchangers [2].In part, due to the high surface area to volume ratio, microchannels permit a high heat transfer rates making them an excellent choice for micro-heat exchangers and microscale cooling systems. Many microfluidic systems and bio-related applications consist of microchannels, e.g., DNA chips and lab-on-a-chip devices [2-3]. In these systems, microchannels are essential for carrying a liquid sample from one position to another and for protecting sensitive micro reactions from being exposed to the environment and becoming contaminated. Moreover, microchannels are usually integrated with various other components such as micro-heat sinks, micro-biochips, micro-reactors, and micro-nozzles [4].

In many MEMS applications, such as micro-pumps and micro-actuators, liquid must often flow through channels with changes in cross sectional area and/or direction

(bends). A number of valveless micro-pumps employ nozzle-diffuser elements (contraction/expansion) in the design, e.g., electromagnetic actuators, and bubble micro-pumps [5]. Nozzle-diffuser elements in micro-pumps utilize the different pressure drop characteristics of the flow through a nozzle and a diffuser to direct the flow in one preferred direction, hence causing a net pumping action. Similarly, serpentine channels with miters bends are often used in rapid mixing of fluid samples in many microfluidic applications such as drug delivery, sequencing or synthesis of nucleic acid, and protein crystallization [6]. Bends can also be used to create flows in T-junctions for fluid mixing.

Understanding the flow phenomenon in microchannels is essential in the design and analysis of microfluidic systems. Abrupt changes in geometry, such as sudden contractions, expansions and 90°miter bends, often result in flow separation and the formation of vortices, inducing an additional loss to the flow. Thus, a systematic study dealing with these different microchannel configurations will provide helpful insight into the flow physics. In addition, the study will also provide vital information that may be applied to the design and analysis of micro-fluidic devices.

Effective design of microfluidic systems containing microchannels requires knowledge of the characteristics of fluid flow in microchannels, including straight, contraction/expansion and miter bend microchannels. Straight microchannels with circular and noncircular cross section have been studied extensively over the last twenty years. Unfortunately, there are limited experimental data on single-phase flow characteristics in microchannels with sudden contractions, expansions and miter bends. The work reported herein was designed to produce data for the fluid flow characteristics in rectangular xurographic microchannels at 90° miter bends containing

contraction/expansion legs. This type of geometry could be utilized in many microfluidic systems, including a continuous flow Polymerase Chain Reaction (PCR) device with two different channel widths for heating and cooling processes.

1.2 Introduction to Xurographic Manufacturing

For the past decade, the development of microfluidic systems based on MEMS technology has attracted scientific and industrial attention. The early developments were mostly based on conventional semiconductor materials and techniques originally developed for the integrated circuit industry [7]. The common material used for these microfluidic systems is silicon because of its ability to create high precision geometries. Other materials used, in brief, include polydimethylsiloxane (PDMS), acrylic, other organic polymers, and glass [8]. The use of these materials and techniques for developing microfluidic devices has typically resulted not only in high cost but also many limitations on fabrication, packaging and testing. Moreover, a large number of microfluidic applications do not require high precision; thus, it is often an unnecessary financial burden to employ traditional micromanufacturing methods.

As the demand for microfluidic applications increases, rapid prototyping technologies will play an increasingly important role in manufacturing microfluidic devices. Rapid prototyping is advantageous over traditional micro-machining techniques because devices can be fabricated quickly and at lower costs. A recent novel manufacturing technique termed “xurography” has been developed as an effective method for manufacturing microfluidic channels [9]. Xurography is the process of cutting the microchannel designs out of a double sided adhesive tape using a knife plotter. The

cut sections on the tape are then removed and the remaining tape is sandwiched between two glass plates resulting in fully enclosed microchannels. The thickness of the tape determines the height of the channels. Two walls of these microchannels are formed by glass while the other two are a combination of adhesive layers and the polyimide film.

Xurography is advantageous due to its short fabrication time, a lack of dependence on clean room technologies, and low equipment and material costs in comparison to other rapid prototyping techniques, e.g., laser micromachining, micropowder blasting and micromachining with glass or polymer substrates. The initial investment for a cutting plotter (~$4000) is significantly less than the micromachining equipment used in a clean room. These advantages of xurography make it an ideal tool for the development of microfluidic systems in the laboratory.

Unfortunately, xurography is inferior to micromachined channels when precision is considered. With xurography, the same geometric designs and cutting conditions often result in different microchannel widths, due to cutting plotter imprecision. The cutting plotter resolution may be as high as 10μm. In addition, xurographic microchannels manufactured using double-sided adhesive tape are only suitable for low *Re* flows. In the case of high *Re* flow, the fluid inlet pressure must be relatively large to overcome frictional and minor pressure losses through the microchannel. Thus, it is highly probable that the fluid in the microchannel may leak between the glass covers and tape. To reduce leakage, additional force may be applied to the bonds with a mechanical clamping system. This mechanical reinforcement has been shown to enable higher *Re* flows. The design of the clamping system used in this study is discussed in Chapter 3.

1.3 Roughness Characterization of Microchannel Sidewall

The continuum flow physics in microchannels are described using the Navier-Stokes equations; however, early on, a number of publications indicated that flow at the microscale behaves differently than at the macroscale and that the Navier-Stokes equations without modifications were incapable of explaining the phenomena [10]. For flow on the macroscale level, the effect of surface roughness on the flow friction is often characterized by the Moody diagram in which the friction factor is independent of the surface roughness for laminar flow. Over the last 15 years, several reasons have been proposed to explain the observed deviation from macroscale behaviors, including differences between experimental and theoretical conditions, microchannel surface roughness, and measurement errors, e.g., channel dimensions and pressure measurement [11]. Several publications reported that in a microscale system, as the relative roughness becomes large, the roughness effects cannot be ignored [12-13]. For this reason, it is important to characterize the roughness of microchannel sidewalls.

A roughness value can be calculated either on a profile (vertical deviations of the roughness from the mean line, i.e., characterization along a straight line) or on a surface. The profile roughness parameters are more common in roughness characterization in comparison to surface area roughness parameters. There are many different profile roughness parameters in use; however, arithmetic average roughness (R_a) and root mean squared roughness (R_{rms}) are by far the two most common. In this study, the microchannel roughnesses were characterized and presented in the form of R_a and R_{rms}. The arithmetic average roughness, also often known as centerline average roughness, is defined as:

$$R_a = \frac{1}{L}\int_0^L |r(x)|dx \tag{1.1}$$

where L is the evaluation length, x is the distance along the measurement and $r(x)$ is the roughness profile. The root mean squared roughness is defined as:

$$R_{rms} = \sqrt{\frac{1}{L}\int_0^L [r(x)]^2 dx} \tag{1.2}$$

Roughness can be measured using a contact or non-contact method. A contact method involves dragging a measurement stylus across the surface. Instruments that can provide contact roughness measurements include a stylus profilometer, an atomic force microscope (AFM) and a scanning tunneling microscope (STM). Non-contact surface roughness instruments, such as an interferometer, confocal microscope, scanning electronic microscope and optical profilometers, avoid surface damage caused by the contact between the stylus and sample surface. In this study, the roughness of microchannel sidewalls was characterized using a Zygo optical profilometer with vertical resolution of 0.1nm. Roughness measurements of the microchannel assemblies could not be obtained due to sample size constraints of the profilometer. Therefore, a set of six smaller xurographic samples were fabricated for roughness measurement. The design and fabrication processes for these samples are discussed further in Chapter 4.

1.4 Microchannel Characterization

Characterization of channel dimensions plays a critical role in assessing the fluid flow behaviors in microchannels. The high uncertainty in some of the previously reported flow studies makes it difficult to generalize the fluid flow behaviors in these

microchannels. It is well understood that the uncertainty in measuring the dimensions associated with hydraulic diameter have the greatest impact on the uncertainty of the Poissuille number [14]. Thus, accurate measurements of hydraulic diameter, or more specifically the channel width and depth, are necessary and play a critical role in the analysis of fluid flow characteristics.

The xurographic microchannels with rectangular cross section were characterized using nondestructive methods under conditions representative of the actual experiments. Width and length measurements were obtained using a Nikon V12A profile projector using a 100x magnification lens with resolution of ±1 μm. The use of glass on two surfaces of the microchannel allows the length and width measurements to be visibly measured under a microscope. Because the microchannels were compressed by a clamping system during the experimentation, the depth measurements of the microchannel were made using laser interferometry with the clamping system in place. Laser interferometry has a low relative uncertainty (less than 0.2%) when obtaining depth measurements for channels with depths on the order of 100 μm. Detailed descriptions of the characterization of microchannel depth, width and length are discussed in Chapter 3.

1.5 Head Loss in Xurographic Microchannels Flow

The fluid flow through any microfluidic system may pass through different geometries. In the course of this flow, the fluid may encounter sudden changes in direction in the form of bends and also sudden changes in flow cross sectional area. These abrupt changes cause fluid to transform the various forms of energy associated with the flow. These energy transformations associated with flow separation and vortex

formation produce pressure losses in the fluid. The loss associated with changes in flow area, such as that in a contraction, expansion, 90° miter bend, elbow, fitting and valve, are classified as minor losses. These losses are classified as minor since the loss due to change in flow geometry is typically smaller in comparison to the frictional loss, which is considered the major loss. For very long conduits, the minor loss is usually insignificant in comparison to the major loss. However, for short pipes, the minor loss may contribute significantly to the total loss of the flow.

The study of friction factor and frictional pressure drop has received considerable attention in the field of MEMS and microfluidic systems. Prediction of these effects is very beneficial in engineering design, in that the designers can actually use and reference available correlations and data without performing the otherwise necessary experimentation to obtain the desired information. Minor loss is generally expressed in one of the two ways: (i) in terms of the minor loss coefficient K, or (ii) in terms of equivalent length of straight channel L_e. The minor loss coefficient K and equivalent length L_e are related to minor head loss h_{Lminor} by the relationships expressed in equations 1.3 and 1.4, respectively:

$$h_{Lminor} = K\frac{\overline{V}^2}{2} \tag{1.3}$$

$$h_{Lminor} = f\frac{L_e}{D_h}\frac{\overline{V}^2}{2} \tag{1.4}$$

where $\overline{V}$ is the average fluid velocity, D_h is the hydraulic diameter, and f is the friction factor. The major head loss h_{Lmajor} is determined by:

$$h_{Lmajor} = f\frac{L}{D_h}\frac{\overline{V}^2}{2} \tag{1.5}$$

where *L* is the length of the channel.

As the flow passes through the change in flow areas, the kinetic energy coefficient, β, must be considered so that the average velocity at the cross section may be used in the kinetic energy term. β is determined by

$$\beta = \frac{\int_A \rho V^3 dA}{\overline{V}^2 \dot{m}} \tag{1.6}$$

where $\overline{V}$ is the velocity field, *A* is the cross section area, $\dot{m}$ is the mass flow rate, and ρ is the fluid density. The head losses along with the kinetic energy coefficient are combined in the energy equation (often called Modified Bernoulli equation) for the channel;

$$\frac{P_1}{\rho} + \beta_1 \frac{\overline{V_1}^2}{2} + gz_1 = \frac{P_2}{\rho} + \beta_2 \frac{\overline{V_2}^2}{2} + gz_2 + h_{Lmajor} + h_{\mathrm{Lminor}} \tag{1.7}$$

where z is elevation and P_1 and P_2 are the static pressures at upstream and downstream locations in the flow, respectively.

Xurographic microchannel fabrication often exhibits variation in channel width before and after an abrupt corner such as a 90° miter bend. The current study is designed to characterize the minor head loss in 90° miter bends containing either a contraction or expansion leg on the downstream side of the bend in rectangular xurographic microchannels. In addition to the change in channel width at the bend, the effect of channel aspect ratio on loss coefficient is also studied. For comparison, experimental data

for frictional losses and critical Reynolds number (Re_{cr}) in straight xurographic microchannels is also obtained. All these data, including friction factor, critical Reynolds number and minor head loss, are compared to data from previous studies.

1.6 Summary

Xurography is an inexpensive rapid prototyping technology that uses a knife plotter to cut various microfluidic designs out of a polyimide film. The advantages of relatively fast fabrication and low equipment and material costs make it ideal for development of microfluidic systems in the laboratory. In addition to small variations in width in straight sections, microchannels fabricated by xurography often exhibit significant differences in width before and after abrupt corners. The goal of this research is to study the characteristic of fluid flow in rectangular xurographic microchannels. The study focuses on characterizing the effect of contraction/expansion in 90° miter bends. The minor loss, frictional factor and critical Reynolds number are reported.

A literature review of relevant data for fluid flow characteristics at the microscale is presented in Chapter 2. Methods and procedures for the experiment are discussed in Chapter 3. Chapter 4 provides a summary of roughness characterization for the microchannel sidewalls and microchannel defects. The presentation of experimental results and discussion are in Chapter 5. Finally, Chapter 6 provides conclusions and recommendations associated with the study.

CHAPTER 2

BACKGROUND AND LITERATURE REVIEW

The background and literature related to this study are reviewed and presented in four separate sections. The first section summarizes some general remarks about microchannels. This section is followed by a review of flow characteristics in straight microchannels. The third section is a review of the experimental and computational works on minor loss coefficient through contraction/expansion and 90° miter bends in microchannels. The final section summarizes the review.

2.1 General Remarks about Microchannels

The term "microchannel" is often used to refer to channels whose inner diameters range from 50 μm to 1000 μm. However, this size range seems too wide; some researchers have proposed their own definitions of microchannels. Kandlikar et al. [15] classified the range of diameters from 1 nm to 10 μm as nanochannels, 10 μm to 200 μm as microchannels, 200 μm to 3 mm as minichannels and greater than 3 mm as conventional channels. Depending on different applications, the channel dimensions are sized differently. Most biological systems employ much smaller channel dimensions than other applications such as micro heat exchangers, micropumps or microturbines.

Fluid flow through a microchannel was first proposed and demonstrated as a means of dissipating heat from an integrated circuit by a Stanford graduate student and his professor, David Tuckerman and Fabian Pease [16]. A microchannel with a 50 μm

width and a 300 μm depth was etched in silicon and water, acting as a coolant, was pumped through the channel 790 W/cm^2 of heat was dissipated when the corresponding substrate temperature was 71°C higher than the inlet water temperature. This novel discovery led to a number of innovative designs and spawned extensive research in the field of microchannel cooling for electronic devices.

The compactness and high surface to volume ratio of microchannels make them attractive alternatives to conventional flow systems for heat transfer enhancement in numerous applications. A specific example for these applications is a micro heat exchanger. Micro heat exchangers have thin separation walls between the fluids where heat is conducted and high channel surface area relative to the volume of fluid resulting in high heat transfer rates for the system. Roy et al. [17] designed and fabricated a micro heat exchanger that consisted of rectangular microchannels with dimensions of 0.5 x 12 mm. The micro heat exchanger was used for cooling semiconductor laser diode arrays, and was capable of dissipating a very high heat flux on the order of 1000 W/cm^2. The overall thermal resistance was less than 0.03 W/°C which was stated to be an improvement of two to three times over other state-of-art heat sinks.

Recently, there has been a growing interest in developing microfluidic devices that can manipulate and transport relatively small volumes of fluid [2,18,19]. Microchannels are often used in a variety of devices incorporating single phase flow such as micropumps, microvalves, and microsensors. The field of biological and life sciences also benefited from these microchannel applications for analyzing biological materials such as proteins, DNA, cells, and chemical agents. The interest in transporting, manipulating, and synthesizing bio-molecules in microchannels is motivated by the

desire to automate biochemical protocols and operate with extremely small samples [15]. A specific example is the field use of a system designed for forensic analysis using small samples of fluids left at a crime scene. In addition, microchannel dimensions also match up well with the scale of biological microstructures and microchannel systems have the potential of multiple functions for chemical analysis [19].

For the past two decades, a flurry of research has been conducted on the flow characteristics in microchannels, with numerous studies appearing each year. The fluid flow characteristics in microchannels have been reported for both laminar and turbulent regimes. Single phase and two phase flows in microchannels have been investigated and reported [10,14,20,36]. These studies are very beneficial as they enable the proper design of microfluidic systems.

2.2 Flow Characteristics in Straight Microchannels

Flow through a straight channel is the most common and simple configuration in a microfluidic system. The flow physics in microchannels are described using the Navier-Stokes equations; however, early on, a number of publications indicated that flow at the microscale behaves differently than at the macroscale and that the Navier-Stokes equations without modifications were incapable of explaining the phenomena [10]. Over the last 15 years, several reasons have been proposed to explain the observed deviation from macroscale behaviors, including differences between experimental and theoretical conditions, microchannel surface roughness, and measurement errors, e.g., channel dimensions and pressure measurement [11].

The review prepared by Papastsky et al. [20] provides an excellent summary of laminar single phase flow in microchannels. Based on the available experimental data at that time, they concluded that: (1) microscale flows are different from macroscale flows, but only in the slip regime, (2) the microchannel surface roughness appears to increase the friction factors in nonslip fluid flow, and (3) there is no reliable range of *Re* for turbulence transition. They proposed several sources of error that could be inherent in microscale fluid flow experiments. These sources of error could be the imprecise or inaccurate measurements of channel dimensions that lead to high uncertainties in the results. The uncertainty of pressure sensors and the location of pressure measurements were observed to cause some deviations; in many cases, the entrance and exit effects have been either estimated or neglected. The surface roughness effects were often neglected or not considered at all. In their conclusion, they suggested further investigation over a wider range of *Re* should be studied using microchannels with well characterized dimensions, surface roughness and well-designed experimental methods.

In 1996, Pfund et al. [21] used de-ionized water to measure the pressure drop in microchannels. The channel was etched in unpolished brass with surface roughness of 0.45 ± 0.33μm. They reported that the friction factor was generally higher than the theoretical values. Early turbulent transition was also observed. The experimental work of Qu et al. [22] indicated that the microscale flow deviated from Stoke flow theory. Their channels had trapezoidal cross sections with hydraulic diameter ranging from 51 μm to 169 μm and relative roughness ranging from 3.6% to 5.7%. The Poissuille numbers, defined as the product of friction factor *f* and Reynolds number *Re*, were found

to be 15 to 30% higher than the theoretical values. Early turbulent transition was observed at around *Re* = 1000.

More recently, researchers have shown that the microscale effect is nonexistent for liquid flows, making macroscale theory suitable for modeling fluid flow phenomena at the microscale [14,19,23]. Judy et al. [14] performed an experimental investigation to determine frictional pressure drops for liquid flow through round and square microchannels fabricated from fused-silica and stainless steel over a Reynolds number range 8-2,300. The channel diameters ranged from 15 μm to 150 μm; the tested fluids included: distilled water, methanol and isopropanal. They reported that the friction factor *f* and Poiseuille number *Po* agreed with theoretical predictions.

A number of research groups also have reported that the laminar friction factor for fluid flow in microchannels was in agreement with macroscale predictions [23, 24, 25]. Costaschuk et al. [23] performed an experimental investigation of water flow through an aluminum rectangular microchannel with hydraulic diameter of 169 μm over a Reynolds number range of 230 to 4,740. They reported the friction factors in laminar regimes were in an agreement with theoretical values. The critical Reynolds number was found to be 2,370. Kohl et al. [24] conducted an experiment to determine the pressure drop in straight microchannels whose hydraulic diameters ranged from 25 μm to 100 μm. Ranges of Reynolds numbers were from 4.9 to 2068 for incompressible flows and from 6.8 to 18,818 for compressible flows. They reported that experimental friction factors were in agreement with theoretical values. Thus, friction factors can be accurately obtained from the data for standard large channels. Table 2.1 summarizes a number of studies on fluid flow characteristics in straight microchannels.

Table 2.1: Experimental results of single phase fluid flow in microchannels.

Author	Microchannel		Fluid	*Re*	Po_{exp}/Po_{thry}	Re_{cr}
	Shape	d_h (μm)				
Peng et al [4]	Trapezoidal	237	Water	50 - 2,800		1,500 - 1,800
Judy et al. [14]	Circular and squared	15-150	Water, methanol, Isopropanol	8 - 2,300	0.82 - 1.27	~2,000
Kolekar [19]	Rectangular	138 - 152	Distilled water	250 – 3,500	~1.0	2,250 – 2,600
Costaschuk et al [23]	Rectangular	169	Distilled water	230 - 4,740	~0.994	2,370
Pfund et al. [21]	Rectangular (smooth surface)	128 – 1050	Water	60 - 3,450	1.08 - 1.12	1,700 - 2,200
	Rectangular (rough surface)	Depth 257	Deionized water	60 – 3,450	~1.25	~1,700
Baviere et al. [25]	Rectangular	100 - 200	Water	< 8,000	~1.0	<2,500
Xu el al. [26]	Rectangular	30 - 344	Water	20 - 4,000	1.0	1,500
Wu el al. [27]	Trapezoidal	25.9 - 291	Deionized water		1.0 ± 0.11	1,500 - 2,000
Qu et al. [22]	Trapezoidal	51 - 169	Deionized water	100 – 1,600	1.15-1.3	~1000

Kolekar [19] performed an experimental investigation on characteristics of water flow in rectangular xurographic microchannels. He reported that the average Poissuille numbers in fully-developed laminar flow were in excellent agreement with Stokes flow theory for all tested microchannels. The turbulent transition was reported to have occurred between *Re* of 2250 to 2600. Additionally, the results of Torgerson's [28] work on xurographic microchannels were in good agreement with macroscale theory and correlations. The critical Reynolds number ranged from 1700 to 2300 and was found to be dependent on channel defects such as adhesive droplets and edge imperfections.

In general, the research on fluid flow characteristics performed to date in straight microchannels indicates an agreement with macroscale theory for continuum flows. When deviations from macroscale theory have been reported, explanations include channel roughness, errors in measurements, and noncontinuum effects; however, further investigation is required. The present study examines the flow of water in a straight section of rectangular xurographic microchannels, a type of microchannel that has yet to be tested. Results will be discussed in Chapter 5.

2.3 Minor Losses in Expansion/Contraction and 90° Miter Bends

Flow in microfluidic applications, such as micropumps and microactuators, is often through channels with changes in cross-sectional area and bends. However, flow studies of complex microscale geometries involving expansions, contractions, and bends are limited. Xiong et al. [29] investigated flow characteristics of water in serpentine microchannels with miter bends of varying hydraulic diameter, ranging from 209 to 622 μm. They reported that: 1) induced flow recirculation or separation did not occur for *Re* <

100, 2) vortices appeared and continued to develop for *Re* > 100, and 3) the shape and size of vortices remained nearly constant for *Re* > 1000. Their data indicated that the loss coefficient, *K*, through a 90° bend remained nearly constant when *Re* ranged from 1000 to 1500. In addition, *K* was larger for the smaller channels with flow separation (*Re* > 100-200). Maharudrayya et al. [30] performed CFD simulations for 90° bends with different curvature ratios, aspect ratios and separation distances between bends. Their results indicated that *K* decreased with a decreasing channel aspect ratio α, where $0 \leq \alpha \leq 1$. For low *Re* flows (*Re* < 100), *K* was higher for a gradual bend than a sharp bend. In the absence of flow separation, skin friction dominated the pressure loss, which was higher in the gradual bend due to its longer overall length. At high *Re* (*Re* > 500), the losses resulting from flow separation dominated; thus, the sharp bend *K* was significantly higher than that for a smooth bend.

To determined the loss coefficients, Herwig et al. [31] also performed CFD simulations for channels with a 90° bend and three 90° bend combinations over a *Re* range from 4 to 512. They reported that the loss coefficient for a 90° bend decreased with increasing *Re*. Haller et al. [32] investigated the pressure loss and heat transfer in microchannels with 90^o bends and branches over a range of *Re* from 10 to 3000. Due to convergence issues with the numerical simulation at high *Re*, numerical simulations were only used for *Re* < 500 and experiments were conducted for higher *Re*. From the simulation results, they reported that the 90° miter bend produced significantly higher pressure loss than the 90° bend with radius; one pair of vortices was noticed for all shapes. Similarly results were observed for *Re* > 500 for the experiment; the 90° bends with radius had a 25 to 28% lower pressure loss in comparison to 90° miter bends. Lee

et al. [33] studied argon gas flow in microchannels with 90° miter, curved and double-turned bends. All microchannels were 20 μm wide and 1 μm deep. They found that the lowest flow rate was measured in the miter bends, thus indicating that the higher loss was in this feature. They also reported the possibility of flow separation in the miter bend microchannel even in the creep flow regime.

Yu et al. [11] performed an experimental study to determine the loss coefficient due to abrupt expansion and contraction in minichannels with diameters ranging from 330 to 580 μm over a *Re* range of 733 to 7941. They reported that loss coefficients through an expansion were invariant with *Re* for laminar flow. *K* through a contraction decreased with increasing *Re* in the laminar region and remained nearly constant in the turbulent region. Zho et al. [34] performed a study to determine the pressure drop in the transition region ($1000 < Re < 5000$) for microtubes (diameters in the range 330 - 850 μm) containing sudden contractions. They reported that the loss coefficients decreased with increasing *Re* for laminar flow followed by an abrupt drop posttransition and remained constant for $Re > 3200$. *K* ranged from 0.4 to 1.5 over the range of $100 < Re < 5000$. This *K* value was consistent with data reported by Abdelall et al. [35].

Chalfi [36] performed an experimental study on pressure drop caused by expansion/contraction in capillaries under low flow condition. The water flowed in two tested capillaries that had diameters of 0.84 mm and 1.6 mm. The Reynolds number covered a range of 160 to 539. He reported the minor loss coefficients for sudden contraction were nearly constant at 0.4 over the range of *Re*, while the minor loss coefficients for sudden expansion slightly increased with *Re*. Costaschuk et al. [23] experimentally investigated entrance and exit minor loss coefficients in microchannels

over $230 < Re < 4740$. This study may be correlated to a contraction and expansion study due to similar geometric conditions. The minor loss coefficients were found to decrease with increasing *Re* for laminar flow, followed by an abrupt drop within the turbulent region for both entrance (comparable to a contraction) and exit (comparable to an expansion) sections in a microchannel. *K* data reported by Costaschuk et al. [23] ranged from 0.5 to 2.0 over $1000 < Re < 4740$. These *K* values were in the range of values reported by Zho et al. [34].

Kolekar [19] performed an experimental study on the characteristics of water flow in straight and 90° miter bends with different aspect ratios in rectangular xurographic microchannels. He reported the minor loss coefficient in a 90° miter bend increased with increasing modified aspect ratio, α_{mod}, defined as the sum of the average aspect ratio for all sections and the average absolute value of the fractional change before and after the 90° miter bends. The loss coefficient was invariant for all channels investigated over $1200 < Re < 2100$. For $Re < 1200$, *K* increased monotonically with *Re* and for flows with $Re > Re_{cr}$ (critical Reynolds number), *K* decreased with increasing *Re*. This variance of *K* with *Re* was explained by the creation of a vortex pair at the bend. Torgerson [28] also performed an experimental study to determine minor loss coefficients through an expansion/contraction in xurographic microchannels. His data indicated that loss coefficients associated with an expansion or contraction decreased gradually with increasing *Re* in the range of 250 to 4000 and increased for decreasing area ratios. The reported loss coefficients through a contraction were significantly higher than data reported by Costaschuk [23]. It is also noted that Torgerson's contraction data were normalized based on specific kinetic energy upstream. Torgerson indicated that

xurographic manufacturing defects correlated with early transition and higher than expected loss coefficients.

2.4 Summary

Numerous studies have been performed to characterize the fluid flow in microchannels over the past two decades. The majority of these studies have concentrated on the fluid behaviors in straight microchannels. The friction factor and the critical Reynolds number have been reported and found to be in agreement with Stoke flow theory, in general. However, only limited data are available for flow through abrupt changes in geometry, such as 90° miter bends, contractions and expansions. Further investigations on these features are necessary.

As discussed previously, both Kolekar [19] and Torgerson [28] reported undesirable channel characteristics due to xurographic plotter imprecision during the cutting process. Microchannel widths were often significantly different (narrower or wider) than the designed dimensions, particularly for orthogonal cuts. The cutter imprecision resulted in microchannels with different widths upstream and downstream of the 90° miter bends. In addition, the plotter was found to be incapable of producing clean cuts at abrupt features such as 90° miter bends. Given these manufacturing concerns, the current study was designed to characterize the effects of a contraction or expansion in a 90° miter bend for microchannels with rectangular cross-section.

CHAPTER 3

EXPERIMENTAL METHODS AND PROCEDURES

The objective of this chapter is to provide a detailed description of microchannel test section designs, fabrication methods and characterization. In addition, a description of the experimental flow loop is presented. The uncertainty analysis and data reduction are also discussed in this chapter.

3.1 Design of Microchannels

As discussed in Chapter 1, the objective of this study was to investigate the effect of contraction/expansion at 90° miter bends on the minor loss coefficient. A total of twelve microchannels were fabricated; six microchannels contained an expansion at the bend and the other six incorporated a contraction at the bend. For each microchannel group (contraction or expansion), three nominal designs of width ratio (ratio of widths before and after the bend) were fabricated. This redundancy enabled repeatability verification of fluid flow behaviors in these xurographic microchannels.

The microchannels were fabricated using the xurographic manufacturing method with a double sided adhesive Kapton® tape and two rectangular glass plates. The microchannels were designed to have a rectangular cross section with different aspect ratios that are dependent on the channels' depth and width. The top and bottom surfaces were formed by two glass plates while the lateral surfaces of the channel were formed by

the surface of the cut tape. Thus, the depth of microchannel was dependent on the thickness of the Kapton® tape, which is approximately 105 μm.

Due to the depth constraint of the channels, the expansion/contraction was controlled by the width of the channels. The microchannel consisted of two straight sections connected by a 90° miter bend; one section was wide and the other narrow. Three static pressures were measured in the flow, two upstream of the bend and one downstream. The first two measurements were used to determine the fully developed frictional pressure drop in the upstream straight section. The first pressure measurement, P_1, was taken 30 mm downstream from the inlet where the flow was fully developed for the entire *Re* range. The hydrodynamic entrance length, L_h, was estimated from macroscale theory [37]; however, it should be noted that the estimates for the entrance length are conservative since researchers have reported smaller L_h for microscale flow in comparison to macroscale predictions [23]. The designed entrance length was also sufficient for turbulent flows [38]. The second pressure measurement, P_2, was taken 15 mm downstream from P_1 and the bend was located 5 mm downstream of the P_2 pressure tap. The third pressure measurement, P_3, was taken 10 mm downstream of the bend. This distance was determined using a correlation by Maharudrayya et al. [30] so that the flow was fully developed after the bend for all *Re*. Finally, the exit port was located 5 mm downstream from the P_3 pressure tap. Square reservoirs, 3 mm on a side, were incorporated at the inlet port, the exit port, and at the end of each pressure tap. The geometries and dimensions of the microchannels are shown in Fig. 3.1.

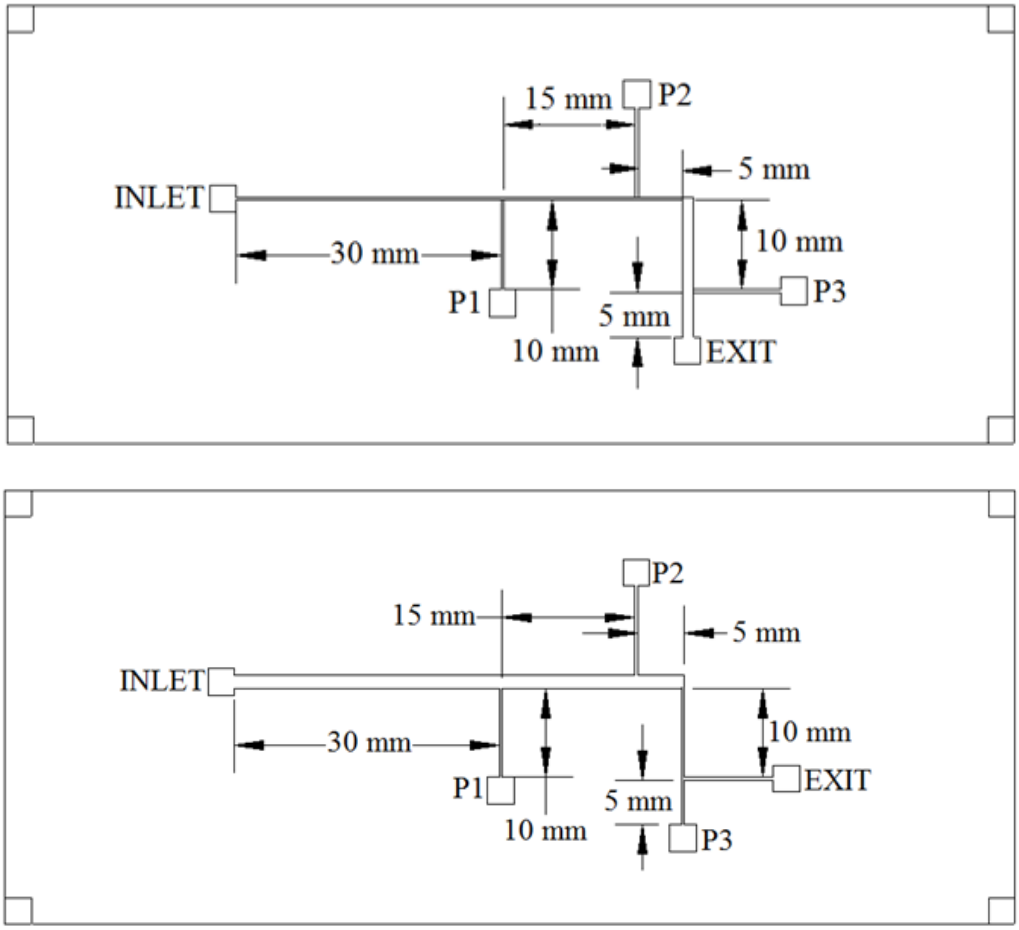

Figure 3.1: Geometry of the microchannel with associated dimensions. The top figure is an expansion microchannel design with 90° miter bend; the bottom is a contraction design. Flow is from left to right. Orthogonal pressure taps are shown in respective locations along the length of the channel, labeled P1, P2, and P3.

The cutting plotter imprecision resulted in channel cuts that deviated significantly from the design dimensions, particularly for the smallest channels. This undesirable characteristic of the cutting plotter will be discussed in more detail in Chapter 4. Throughout the pretests, it was concluded that 300 μm was the smallest nominal width of the channel that resulted in a successful cut and subsequent bonding to form the channel. The channels were designed to have nominal width ratios of 0.5, 0.33, and 0.2. The design expansion/contraction width ratios for the 90° miter bends are shown in Table 3.1.

Table 3.1: Designed expansion/contraction ratio at 90° miter bends

Expansion Design	Inlet Width (μm)	Exit Width (μm)	Ratio*
1	300	600	0.5
2	300	900	0.333
3	300	1500	0.2
Contraction Design	Inlet Width (μm)	Exit Width (μm)	Ratio*
1	600	300	0.5
2	900	300	0.333
3	1500	300	0.2

*Ratios were defined to be less than 1.

3.2 Microchannel Fabrication Using Xurography

The processes of microchannel fabrication using the xurographic manufacturing method are discussed in this section. The microchannel fabrication can be divided into four separate processes: 1) channel design using *Adobe Illustrator* 2) glass drilling and nanoport bonding process, 3) cutting plotter process and 4) the final microchannel assembly.

3.2.1 Channel Design Using *Adobe Illustrator*

In preparation for the plotting, the microchannels were designed graphically using computer aided design software. *Adobe Illustrator* is the computer program of choice for microchannel design as this program interfaces well with all cutting plotters. The microchannel drawings can be created directly using *Adobe Illustrator* and sent to a Graphtec cutting plotter. *AutoCAD* or *Solidworks* may also be used for designing microchannels; however, the design files would need to be converted to a *.dxf* file and imported to *Adobe Illustrator*. Figure 3.1 is an example of a channel design that was

created using *SolidWorks* and converted to *.dxf* files for both expansion and contraction microchannels at a 90° miter bend.

3.2.2 Glass Drilling and Nanoport Bonding Process

Once the design of microchannels has been completed, the process of drilling the glass plate for access holes could be undertaken. The rectangular glass plate had dimension of 114.3 mm (4.5 inches) in length, 50.8 mm (2.0 inches)in width, and 3.2 mm (0.125 inches) in thickness. The locations of the flow inlet, outlet and pressure taps in the design were used as the references for drilling the access holes on the top glass plate as shown in Fig.3.2a. The design was printed on a sheet of paper, and then the glass plate was placed over the printed design and the drill locations were marked on the glass as shown in Fig. 3.2b.

Once the drill locations were marked, the holes were then drilled using a 1.59 mm (1/16 in) diamond coated drill bit that was mounted on a Dremel rotary tool, as shown in Fig. 3.2c. Due to the brittleness of glass, an intermittent drilling sequence in a cold water bath was utilized. The water bath helps dissipate the heat generated by the drilling and reduces the risk of cracking. In addition, by applying an intermittent drilling sequence, the glass was allowed to cool down in the water bath and wear on the drill bit is reduced.

Once the access holes were drilled, the upper glass plate was cleaned with an isopropyl alcohol solution and distilled water, as shown in Fig. 3.2d. The glass plate was left to air-dry completely before the nanoport bonding process began. The glass plate was cleaned to remove all dust and chips from the drilling process which results in improved adherence between the adhesive ring and the glass plate.

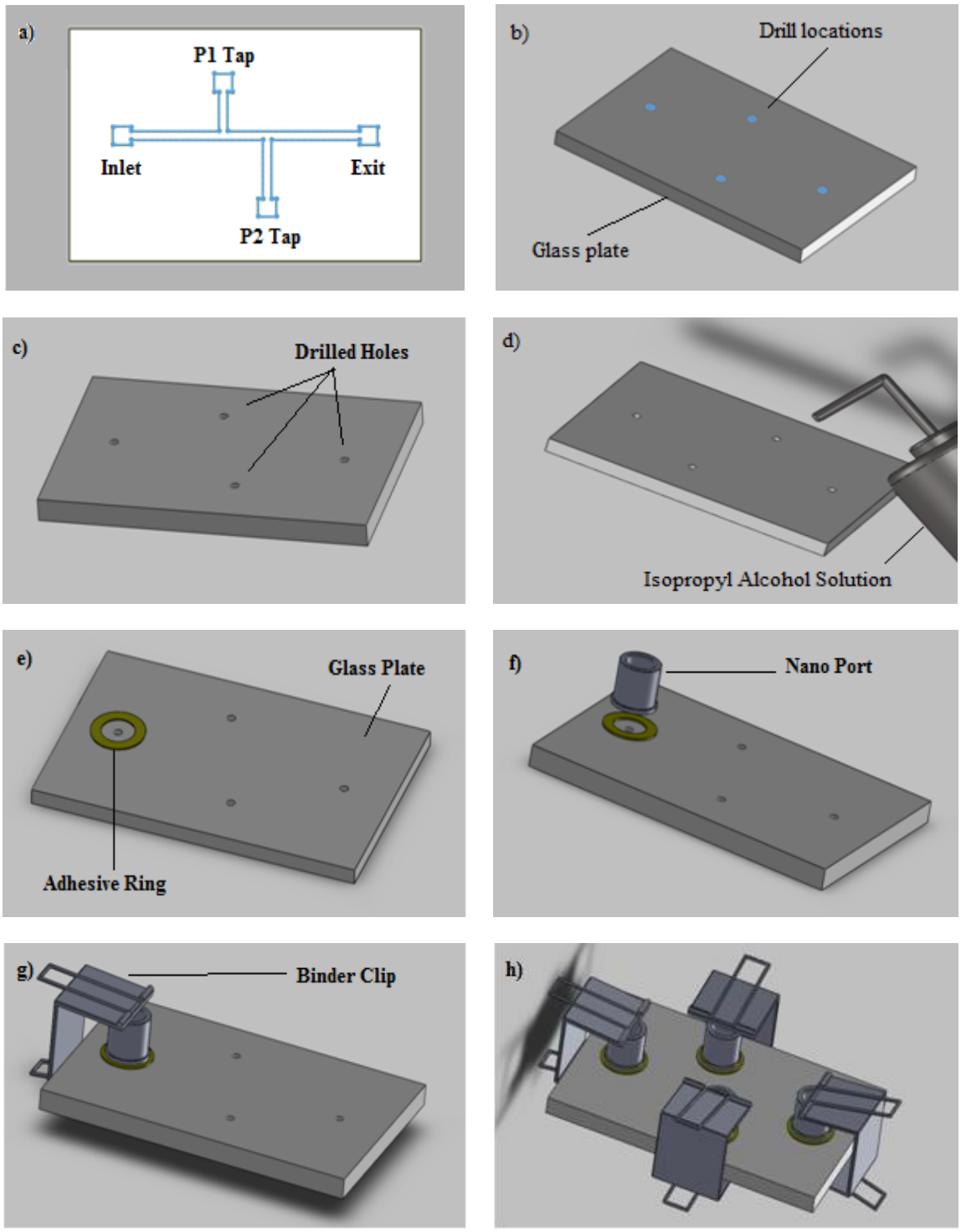

Figure 3.2: Glass drilling and nanoport bonding processes: (a) Microchannel design, (b) Label drilling location, (c) Drill hole, (d) Clean glass plate using isopropyl alcohol solution, (e) Align adhesive ring with drilled hole, (f) Align nanoport with the drilled hole and adhesive ring, (g) Clamp nanoport over the glass using binder clip, (h) Finalize nanoport bonding process to all drilled holes.

Access to the microchannels was achieved by bonding the nanoports to the top glass plate, in alignment with the drilled holes. Each nanoport (Upchurch Scientific Inc.) has a diameter of 1.588 mm. The bonding process started by placing the adhesive ring over the glass plate in alignment with the drilled hole, as shown in Fig. 3.2e. Then, the nanoport was placed on top of the adhesive ring and aligned with the drilled hole, as shown in Fig. 3.2f. A binder clip was used to apply pressure on the nanoport and adhesive ring and to hold them in a fixed location, as shown in Fig. 3.2g. Similarly, the same process was used to bond nanoports onto other drilled holes on the glass plate, as shown in Fig. 3.2h. The final step of this process was to place the glass, adhesive rings, nanoports and binder clips in an oven at 175°C for an hour for curing. During this curing process, the adhesive rings formed bonds between the nanoports and glass plate. The processes of glass drilling and nanoport bonding are shown in Fig 3.2.

3.2.3 Cutting Plotter Process

While the upper plate of the microchannel assembly was being cured, the process of cutting the Kapton® tape was performed. Double sided Kapton® tape has a thickness of approximately 105 µm and consists of three layers: two adhesive layers on both sides of a polyimide film layer. It should be noted that the tape came with a plastic film to protect one side of the adhesive layer.

The Kapton® tape was loaded into a Graphtec cutting plotter with the exposed adhesive layer surface facing up, the protective plastic film surface facing down. The graphical design of microchannel was loaded into *Adobe Illustrator* on a computer, and then sent to the plotter for cutting as shown in Fig. 3a. The cutting plotter automatically

performed the cutting process; the microchannel was cut as shown in Fig 3.3b. Following the cutting sequence, the cut section of tape was removed using a fine point tweezer, as shown in Fig. 3.3c. It should be noted that the tape was initially removed at the square reservoir and then slowly removed from the straight sections. By removing the cut section at the square reservoirs, damage to the channel sidewalls by the tweezers was mitigated. Following the removal process, the remaining tape was observed under a long optical microscope and noticeable adhesive droplets were removed with care using a fine point tweezer, as shown in Fig. 3.3d. The remaining tape was placed on a clean surface with the exposed adhesive layer facing up. This step minimizes the possibility of the adhesive film collecting dust, hair, and other particles in contact with the surface.

In a separate process, the bottom glass plate was cleaned with isopropyl alcohol solution and distilled water. The glass was left to air-dry completely before adhering it to the Kapton® tape. Failure to properly clean the glass surface can result in poor adherence between the glass surface and adhesive film. The remaining tape was aligned with the clean bottom glass and the exposed adhesive layer was adhered to the bottom glass plate, as shown in Fig. 3.3e. To ensure the adherence between the glass and adhesive film, a roller was rotated over the backside of the tape, as depicted in Fig 3.3f. Once the tape was secured to the bottom glass plate, it was safe to leave as long as necessary before completing the next step of the manufacturing process.

3.2.4 Final Assembly of Microchannels

Once the upper glass plate and nanoports had sufficient time to cure in the oven and cool down to room temperature, the final step was to assemble the top and bottom

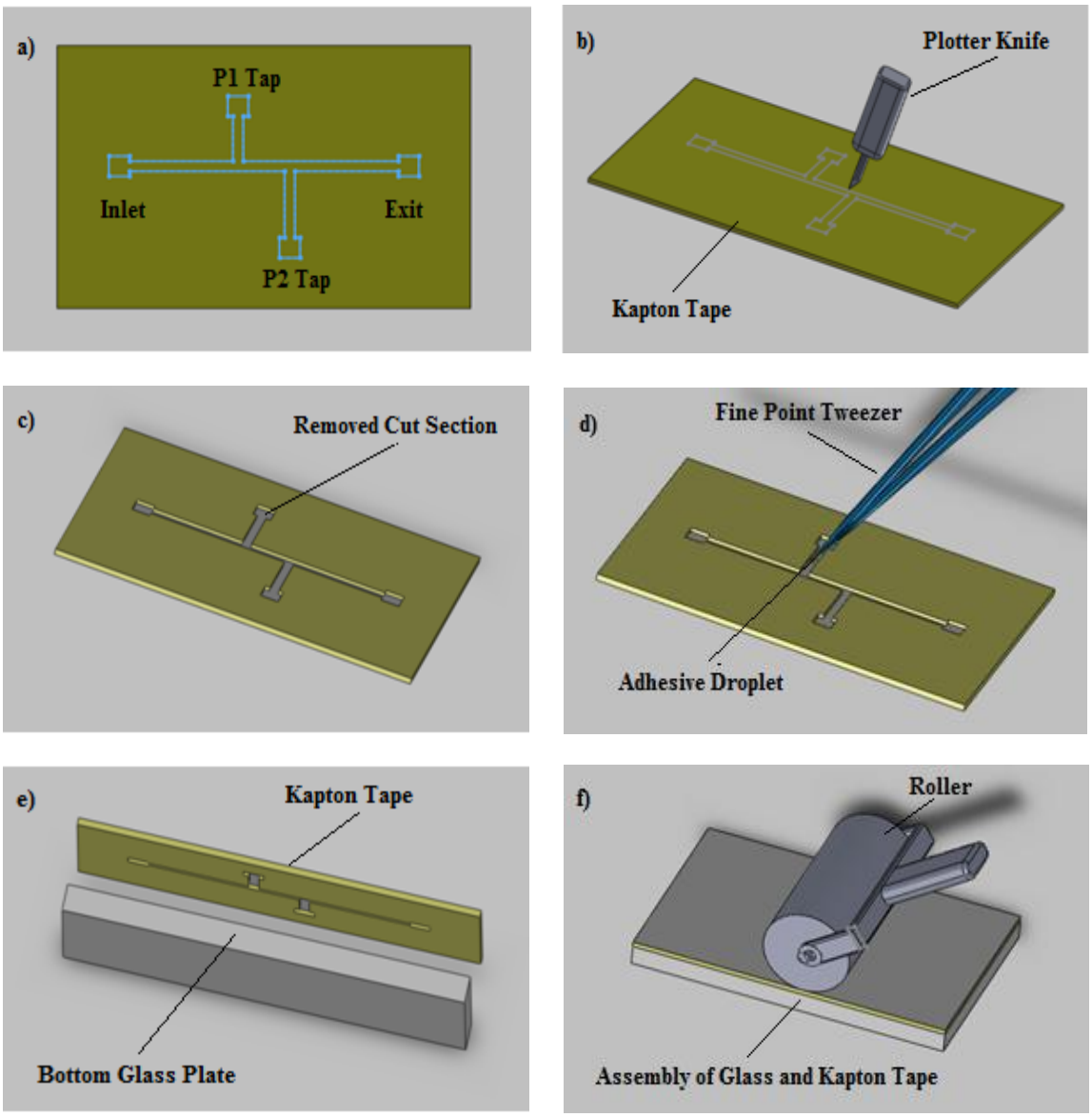

Figure 3.3: Cutting plotter processes: (a) Microchannel design, (b) Cut microchannel pattern in Kapton® tape, (c) Remove cut section (d) Remove attached noticeable adhesive droplets (e) Align remaining Kapton® tape with glass plate (f) Roll on back side of adhered tape.

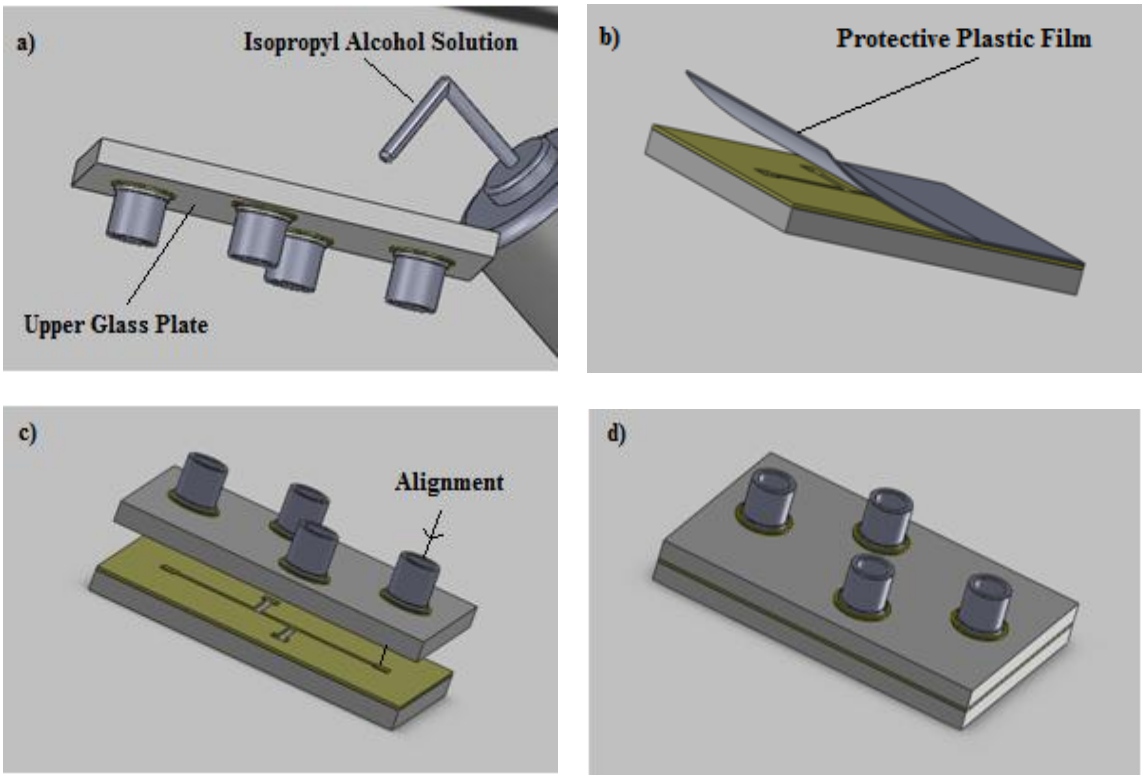

Figure 3.4: Final assembly: (a) Clean upper glass plate, (b) Remove protective plastic film on bottom plate, (c) Align top and bottom plate, (d) Final assembly of microchannel.

glass plates to form a microchannel. The bottom surface of the top glass plate was cleaned and left to air-dry completely, as shown in Fig. 3.4a. This minimizes the dust and other particles introduced to the channel and improves the adherence between the top glass and adhesive layers. The protective plastic film from the bottom plate was removed, as shown in Fig. 3.4b. The top plate was aligned carefully so that the drilled holes on the top plate were in alignment with the square reservoirs on the bottom plate. Figure 3.4c shows this alignment process. To ensure adherence between the two glass plates, manual pressure was applied. The assembly was then placed in an oven at 65°C for about 30 minutes for final bonding between the glass and adhesive layers. Once the assembly cured, the microchannel fabrication was complete, as shown in Fig. 3.4d.

3.3 Mechanical Clamping System Design and Application

Initial testing of the microchannels indicated that leakage occurred due to the high inlet pressures that accompany high *Re* flow. A P_1 pressure of 138-207 kPa (20-30 psi) was sufficient to cause leakage [28]. To alleviate this problem, a mechanical clamping system was designed to apply additional force to the top and bottom glass surfaces of the microchannels, thus enabling an investigation of high *Re* flows. The clamping system was constructed of two 12.7 mm thick polycarbonate plates. Polycarbonate is an excellent choice of material for this clamping system because of its rigidity and transparency. The transparent property made it possible to observe the samples during the experiment. The design of the mechanical clamping system is shown in Fig. 3.5. Note that access holes were also provided for the nanoports. The cuts required for the polycarbonate plate were designed using *SolidWorks* and machined using an automated water jet. Two rectangular PDMS cushioning blocks were inserted between the polycarbonate plates and the microchannel assembly to more evenly distribute the force over the entire microchannel.

The clamping assembly was tightened using a calibrated torque wrench with resolution of 0.113 N-m. A torque of 2.373 N-m was applied on all six bolts in a sequential manner with a torque increment of 0.339 N-m. With a clamping torque of 2.373 N-m, the microchannels were able to sustain a maximum pressure of 3.45 MPa (500 psi) in many cases. For higher *Re* flow, with an accompanying higher inlet pressure, thicker glass plates could be used for the top and bottom surfaces of the microchannel assembly. Thicker glass allows the channel to withstand higher pressure and higher clamping torque. The clamping system and microchannel constituted the microchannel assembly used for testing.

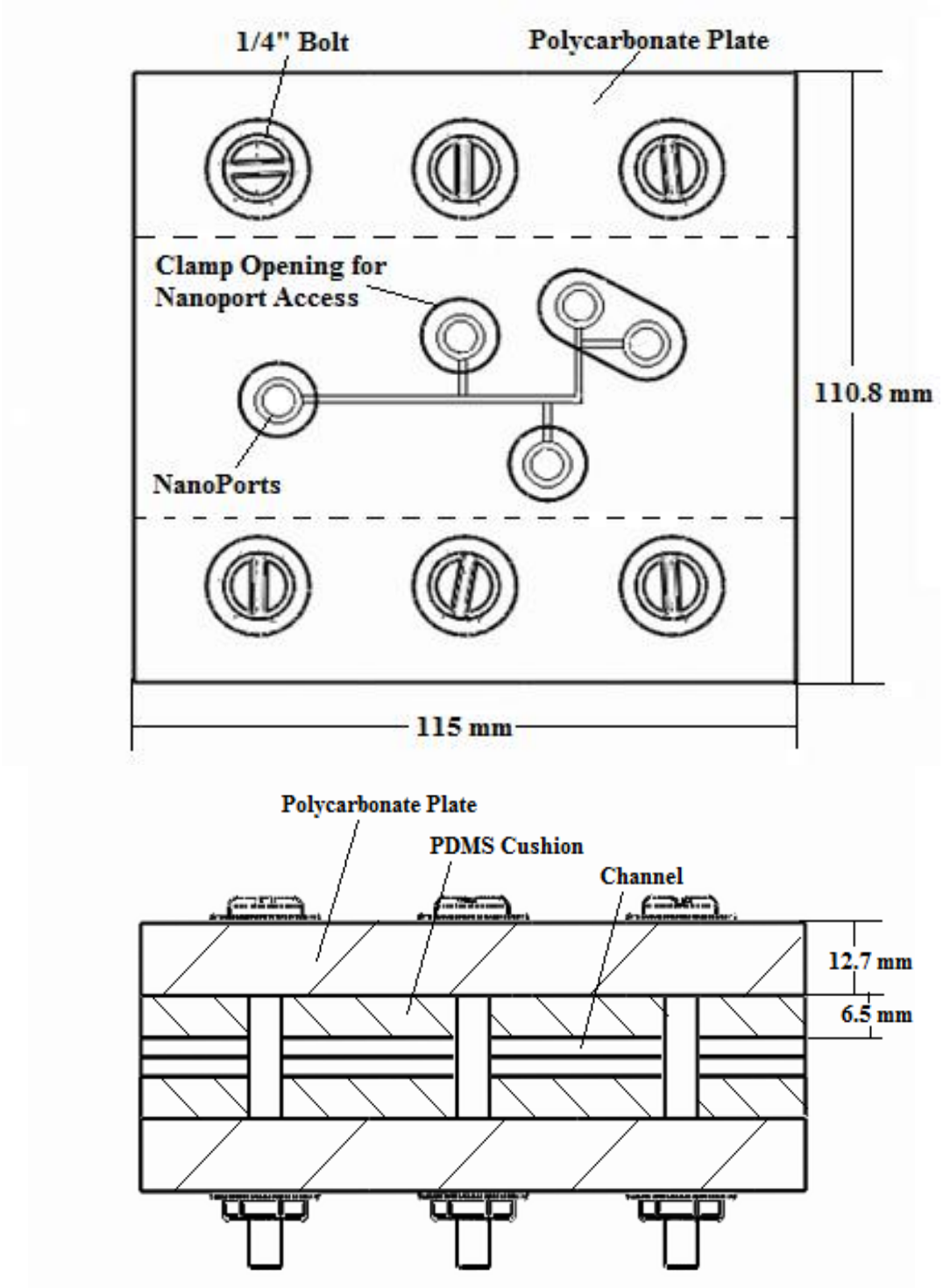

Figure 3.5: Top and side view schematic of mechanical clamping system.

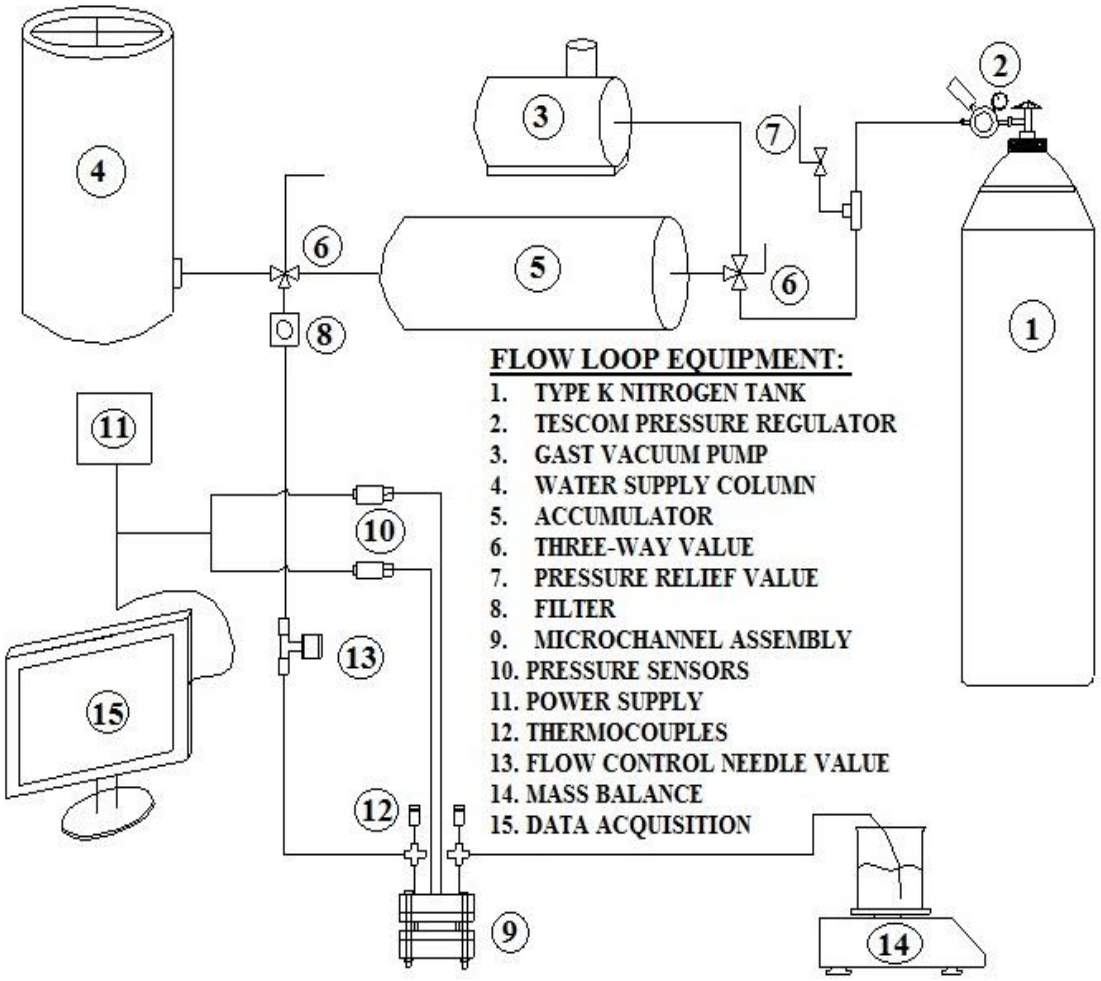

Figure 3.6: Experimental flow loop schematic

3.4 Flow Loop and Test Procedures

Distilled water was used as the working fluid in the open flow loop shown in Fig. 3.6. The water was driven by a Parker piston-type accumulator (3.785 L, 101.6 mm bore) charged with nitrogen gas from a type K nitrogen tank. To minimize gas absorption into the water, the liquid side of the accumulator was separated from the gas side by a stainless steel piston. A Tescom pressure regulator was used to control the applied pressure, thereby providing a nearly constant flow rate to the test section. Two Swagelok

T-valves were used on either side of the accumulator to control the flow of gas and water for accumulator filling and discharge. The water supply column and accumulator were connected using stainless steel tubing (6.35 mm outer diameter).

To fill the accumulator, a Gast vacuum pump evacuated the air side of the accumulator causing water to be drawn from the water supply column into the liquid side of the accumulator. The outlet Swagelok T-valve on the water side was then opened while the accumulator was charged with nitrogen gas, driving the water to the test section. A 7 μm filter removed any impurities contained in the water. A Swagelok needle valve was used for fine-tuning the flow rate. The microchannel was situated between two four-way unions, which were inline with the filter and control valve. The inlet and outlet temperatures were measured at these unions using T-type shielded thermocouples with an uncertainty of ±0.1°C. The four-way unions were connected to the inlet and exit nanoports using P-627 adapters and PEEK tubing (1.588 mm OD). Connections from the nitrogen tank through the accumulator, filter and four-way union were made with PEEK and stainless steel tubing (3.173 mm OD).Static pressure measurements were obtained using Setra 522 series sensors with uncertainty of ±0.15% of full scale. Power for the sensors was supplied by a Kenwood PR36 power supply. The pressure sensors were connected to pressure taps using the same adapters and tubing used for the inlet and exit nanoports.

Upon exiting the four-way union downstream of the microchannel, the water was collected in a plastic beaker (600 g capacity) placed on a mass balance. The mass flow rate was determined using a Scientific SL600 mass balance and internal clock within LabView. The uncertainty in mass and time measurements were ±0.01 g and ±0.01 s,

respectively. The beaker was covered with a Gelman Sciences TF-200 PTFE membrane filter to minimize water loss through evaporation. The mass of water was recorded at regular time intervals controlled by a LabView data acquisition program. The time interval between successive data acquisitions was predetermined based on the approximate mass flow rate. For low mass flow rates, a prolonged time interval allowed more mass to be collected and minimized mass flow rate uncertainty. A National Instruments PX-1010 data acquisition system was used to acquire and record all measured data from the pressure sensors, thermocouples and mass balance. In addition to collecting and displaying real time data such as pressure, temperature, mass and time, a LabView based program was also designed to calculate and display other derived parameters such as Reynolds number, mass flow rate and friction factor.

During the testing, the mass balance was not allowed to exceed 600 grams. If the mass of water approached 600 grams, the experiment was halted and the bottle was emptied. If the accumulator needed to be refilled with water, the experiment was stopped by closing the Tescom valve. Then, the relief valve between the Tescom valve and accumulator was opened to relieve the high pressured Nitrogen gas in the accumulator. The water supply column was filled with distilled water. The three-way values were adjusted in the position for filling the accumulator as discussed above. The water was drawn into the accumulator with assistance from the Gast vacuum pump. The system was then switched back to the testing arrangement and the data collection process was continued.

It should also be noted that the pressure sensors were unexchangeable when the experiment was running. For low *Re* flow, the low range pressure sensors were used. The

use of low pressure sensors at low *Re* flow provided better accuracy in pressure measurements due to their lower uncertainties. For high *Re* flow, the sensors were exchanged for higher range pressure sensors.

In this experiment, the Tescom valve was first adjusted so that the flow obtained a Reynolds number value in the range of 200 to 300. This selection was based on the relative uncertainty of the friction factor, which was estimated to be approximately 10-15% for the initial low flow rate. The flow with *Re* less than 200 had relatively high uncertainties due to the very low flow rate and low pressure drop. Once steady state was achieved, the desired data were recorded and saved in a *.txt* file. Subsequent sets of data were taken for increasing *Re* on the order of 50 to 100 intervals. This change was achieved by slowly adjusting the Tescom valve that controlled the pressure in the accumulator. Data were taken for sets of increasing *Re* until the upper limit of the pressure sensor was reached or the channel failed due to leakage or cracking.

3.5 Characterization

Characterization of channel dimensions plays a critical role in the analysis of fluid flow behavior in microchannels. High uncertainties in the reported flow characteristics can make it difficult to generalize the fluid flow behaviors in these microchannels. The hydraulic diameter, D_h, accounts for the largest uncertainty in friction factor, Reynolds number and Poissuille number. Thus, accurate measurements of microchannel dimensions are necessary. The characterization performed on the microchannels included measurement of length, width and depth and a measurement of sidewall roughness. Contrary to most microscale studies in which microchannel dimensions are measured

during the fabrication process or posttest using a destructive method, the microchannels in this study were characterized using nondestructive methods under conditions representative of the experimental conditions.

3.5.1 Length and Width Measurements

Width and length measurements were obtained using a Nikon V12A profile projector using a 100x magnification lens with ±1 μm resolution. Fifteen and 10 width measurements were taken upstream and downstream of the 90° bend, respectively. The width and length measurements were made in an unclamped condition since it was determined that the relative difference in width with and without the clamping system was negligible [28].The microchannel was placed under the magnification lens, and the top of the channel was brought into focus by adjusting a z-knob on the projector. The width measurements were taken by traversing the channel from one cut edge of the tape to the other. The measurements were displayed on a Quick Chek Control that was connected to the projector. Figure 3.7 represents a photograph of the set up of a Nikon V12 profile projector. Mean width values upstream and downstream of the bend for each microchannel are reported in Table 3.2 Standard deviation for the width measurements for all twelve microchannels ranged from 1.23 to 4.62 μm. Microchannel lengths and separation distance between pressures taps were measured in the same manner. Length measurement for the three sections L_1 (distance between P_1 and P_2 pressure taps), L_2 (distance between the P_2 pressure tap and the bend) and L_3 (distance from the bend to the P_3 pressure tap) are also reported in Table 3.2.

Table 2: Microchannel characterization data, where *b* is the bend location

		$\alpha_{entrance}$	α_{exit}	$D_{h,\,entrance}$ (μm)	$D_{h,\,exit}$ (μm)	$W_{entrance}$ (μm)	W_{exit} (μm)	H (μm)	$1/A_R$	L_{12} (mm)	L_{2b} (mm)	L_{b3} (mm)
BEND WITH EXPANSION	A	0.429	0.181	146.62	177.37	244.25	578.22	104.75	2.23	15.03	5.01	10.01
	B	0.400	0.180	149.16	176.98	261.23	581.32	104.38	2.08	15.01	5.00	10.02
	C	0.434	0.116	144.37	185.54	238.50	893.45	103.52	3.68	15.02	4.99	9.99
	D	0.420	0.119	148.30	188.13	250.82	883.71	105.27	3.47	14.99	5.02	10.01
	E	0.395	0.070	149.04	194.27	263.12	1479.56	103.96	5.46	15.02	5.01	10.02
	F	0.435	0.071	145.49	195.04	239.80	1476.08	104.42	6.12	15.01	4.98	10.00
BEND WITH CONTRACTION	A	0.189	0.349	174.66	153.88	550.13	297.27	103.81	1.87	15.01	4.98	9.98
	B	0.191	0.337	177.47	158.00	554.25	313.18	105.65	1.83	15.06	502	10.02
	C	0.115	0.326	185.91	156.32	902.36	318.03	103.63	2.84	14.97	5.04	9.99
	D	0.123	0.294	186.55	161.81	854.21	355.92	104.71	2.45	14.99	5.01	10.01
	E	0.071	0.318	195.23	158.69	1470.10	329.02	104.56	4.48	15.01	4.99	10.00
	F	0.071	0.374	196.55	153.16	1481.03	281.07	105.26	5.27	14.97	4.98	9.99

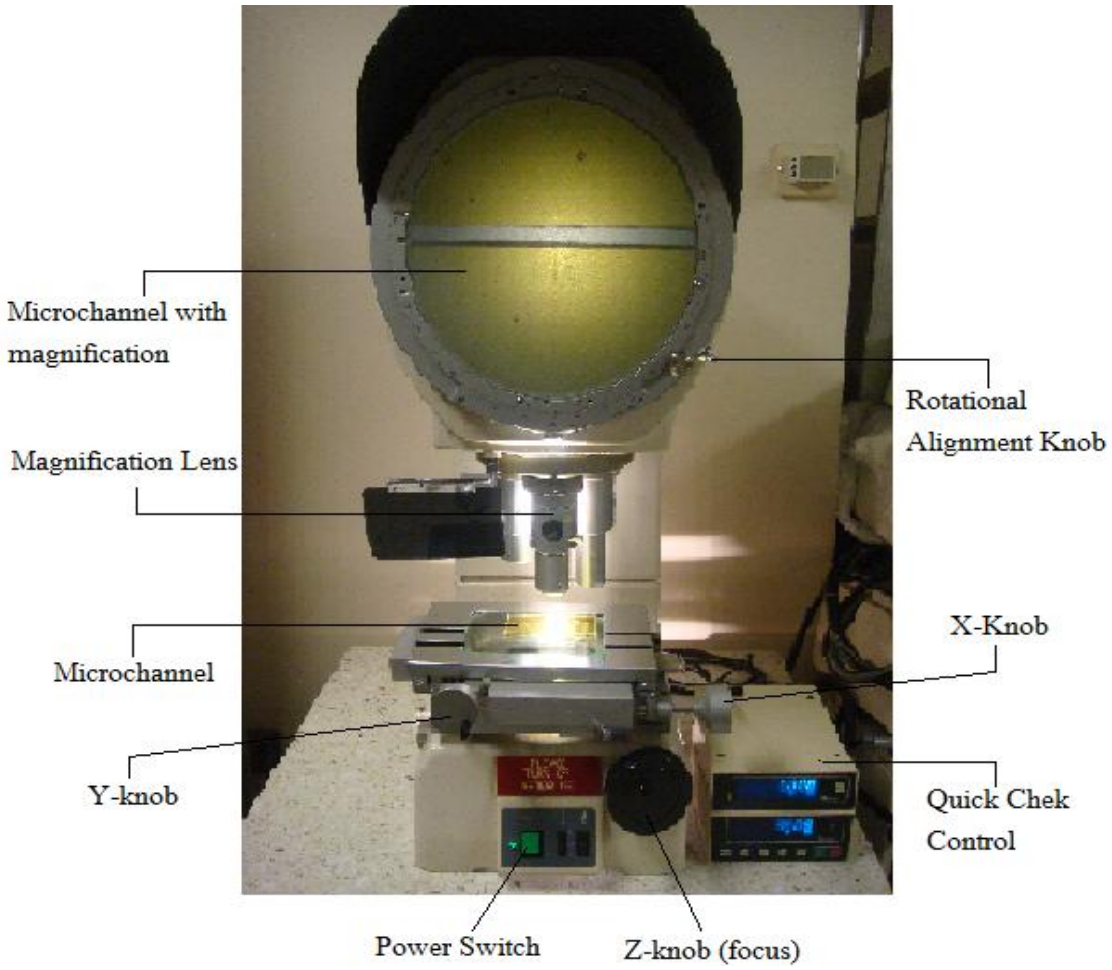

Figure 3.7: Photograph of length and width measurement set-up using Nikon V12A profile projector.

3.5.2 Depth Measurements

Due to the significant adhesive layer thickness (~80 μm), the depth of xurographic microchannels can change significantly when clamped. Therefore, depth measurements were made using laser interferometry with the clamping system in place. Figure 3.8 represents a photograph of the equipment arrangement for laser interferometry depth measurement. Laser interferometry is the most accurate and inexpensive, nondestructive technique, for characterizing the depth in transparent microchannels [19]. Laser

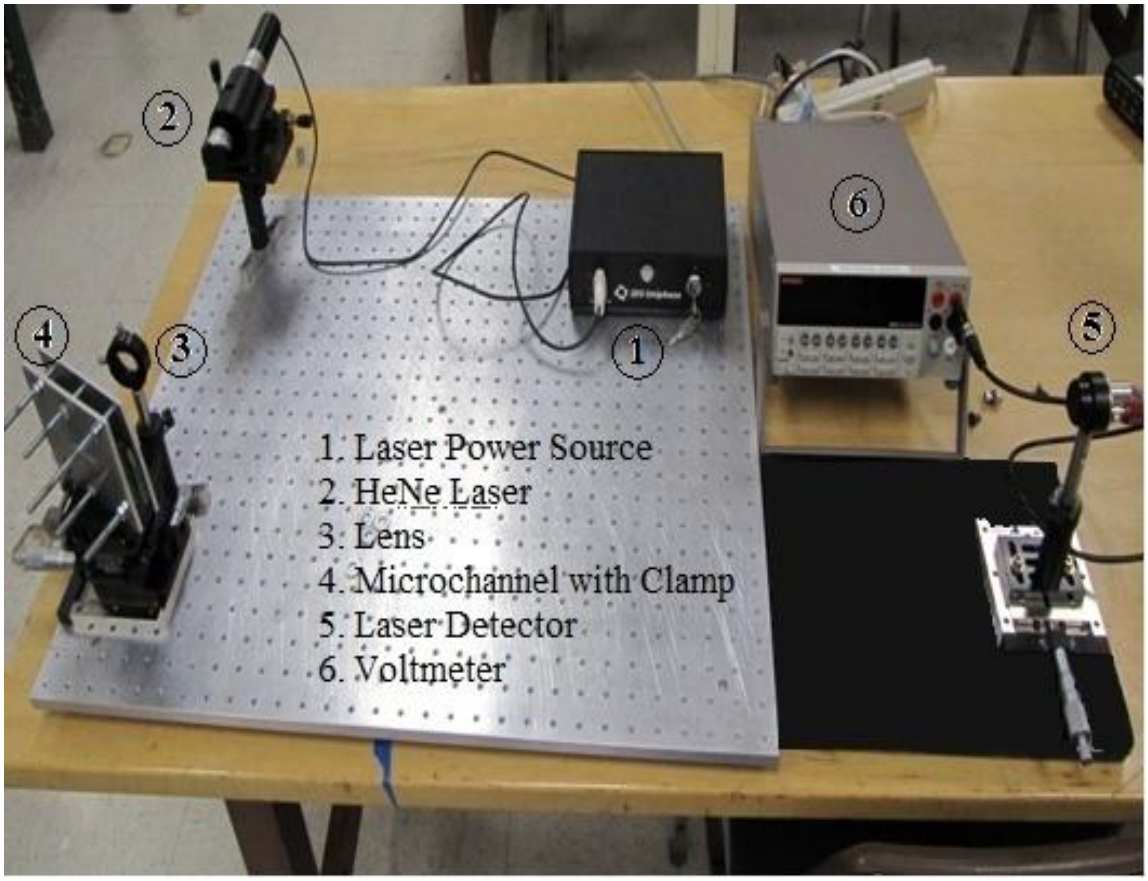

Figure 3.8: Photograph of depth measurement set-up using laster interferometry.

interferometry has a low relative uncertainty (less than 0.2%) for microchannel depths on the order of 100 μm. The uncertainty in depth measurements was based on the uncertainty of all measured variables, which included the distance between a known number of fringes, *x*, the distance between the focal point of the beam and the center of the fringe pattern, *L*, and the angle of incidence, θ. The measurement uncertainties of these three variables were 0.005 mm, 0.5 mm and 0.0417°, respectively. A detailed description of the laser interferometry technique applied to microchannels can be found in Kolekar [19]. Fifteen depth measurements were taken at evenly spaced locations along the microchannel length. Only one depth measurement was taken at each axial location.

The mean depth for all 12 microchannels is between 103.52 and 105.65 μm, while the standard deviation ranged from 0.267 to 0.907 μm. The mean depth, aspect ratio, area ratio, and hydraulic diameter upstream and downstream of the bend for each microchannel are presented in Table 3.2.

3.6 Data Reduction

The experimental data were utilized in a Matlab code to determine the Reynolds number, friction factor and minor loss coefficient along with their associated uncertainties. Experimental data were selected by first determining the time interval between mass measurements such that uncertainty in the mass flow rate was less than 0.15%. The method of calculating relative uncertainty will be discussed later in the uncertainty analysis section. Pressure and temperature data were averaged for the selected time interval.

The density and dynamic viscosity of water were assumed to be functions of temperature only and were computed using the average of the inlet and exit temperatures. Water density as function of temperature was determined from a fifth order polynomial curve fit of the data valid for a temperature range of -20 to 40°C, as presented by equation 3.1 [39]. Similarly, dynamic viscosity as function of temperature was computed using a fifth order polynomial curve fit of the data in the temperature range of 0 to 50°C, as presented by equation 3.2 [39].

$$\rho = (1.4385\times10^{-8})T_{avg}^{5} - (1.8895\times10^{-6})T_{avg}^{4} + (1.2318\times10^{-4})T_{avg}^{3} - (9.2686\times10^{-3})T_{avg}^{2} + (6.6821\times10^{-2})T_{avg} + 999.8748 \quad (3.1)$$

$$\mu = -(1.3109\times10^{-12})T_{avg}^{5} + (2.7464\times10^{-10})T_{avg}^{4} - (2.5655\times10^{-8})T_{avg}^{3} - (1.4718\times10^{-6})T_{avg}^{2} - (6.039\times10^{-5})T_{avg} + 1.7866\times10^{-3} \quad (3.2)$$

where T_{avg} is the average of the inlet and exit temperatures in °C, ρ is the density of water in kg /m^3 and μ is the viscosity of water in Ns/m.

The Reynolds number is defined as the ratio of inertial and viscous forces,

$$Re = \frac{\rho V D_h}{\mu} \quad (3.3)$$

where μ and ρ are computed using equation 3.1 and 3.2, respectively, V is the mean velocity determined from the mass flow rate, and D_h is the hydraulic diameter of the channel. The hydraulic diameter is defined as $D_h=2H*W/(H+W)$ where H is the depth and W is the width of the channel.

The friction factor, f_{exp}, in the entrance section was determined using the pressure difference between the two static pressure measurements P_1 and P_2. f_{exp} for the microchannel is:

$$f_{\exp} = \frac{2\Delta P}{\rho V^2}\frac{D_h}{L} \quad (3.4)$$

where ΔP is the pressure difference between pressure taps 1 and 2 and L is the length between pressure taps 1 and 2.

The theoretical Poiseuille number, Po_{thry}, for incompressible, laminar flow in a rectangular channel was determined using a correlation presented by Shah and London [40]:

$$Po_{thry} = f_{thry}Re = 96\left(1-1.3553\alpha+1.9467\alpha^2-1.7012\alpha^3+0.9564\alpha^4-0.2537\alpha^5\right) \quad (3.5)$$

where α is the channel aspect ratio defined as $\alpha = H/W < 1$. The pressure drop between pressure taps 2 and 3 is designated ΔP_{23}. The total minor loss associated with the 90° bend, expansion, and development loss was obtained using the head-loss equation presented by Fox and McDonald [38]. This analysis resulted in the following equation:

$$\frac{\Delta P_{23}}{\rho} + \frac{\beta_2 V_2^{\,2}}{2} - \frac{\beta_3 V_3^{\,2}}{2} = f_{exp}\frac{L_{2b}}{D_{h,2}}\frac{V_2^2}{2} + f_{thry}\frac{L_{b,3}}{D_{h,3}}\frac{V_3^2}{2} + K_e\frac{V_2^2}{2} \tag{3.6}$$

where b is the spatial location at the bend, f_{thry} is calculated from equation 3.5, K_e is the expansion loss coefficient, $u(x,y)$ is the streamwise velocity profile, and β is the kinetic energy coefficient defined as:

$$\beta = \frac{\int_A u(x,y)^3 dA}{AV^3} \tag{3.7}$$

Note that the friction factor for the section between b and pressure tap 3 was obtained from equation 3.5 since earlier work in similar xurographic channels indicated that the experimental and theoretical friction factors were in agreement [41]. This approximation greatly simplified the channel design since a fourth pressure tap was not required. Equation 3.6 was also used to determine the loss coefficient for a contraction, $K_{c,}$ which is defined as the total minor loss for a 90° bend, contraction, and flow development length. For the contraction, however, the specific kinetic term for the minor loss in equation 3.6 was based upon V_3 instead of V_2. Minor loss data for contractions are presented only for laminar flow, both upstream and downstream of the bend. For laminar flow, β was calculated using the analytical streamwise velocity profile for a duct as a function of channel size and α [40]. For turbulent flow, β was assumed to be equal to 1.0 [42]. Based

upon the laminar flow data presented by Maharudrayya et al. [12], it was assumed that the flow had redeveloped at pressure tap 3. It is important to note that the additional loss associated with development length for the flow to redevelop after the bend was not accounted for in equation 3.6. Therefore, the minor loss coefficients presented in this paper include this development loss.

3.7 Uncertainty Analysis

The uncertainty for a quantity R that is the function of measurements $x_1, x_2, \ldots x_n$ is defined as:

$$\delta Q = \left[\left(\frac{\partial R}{\partial x_1} \partial x_1 \right)^2 + \left(\frac{\partial R}{\partial x_2} \partial x_2 \right)^2 + \ldots\ldots\ldots + \left(\frac{\partial R}{\partial x_n} \partial x_n \right)^2 \right]^{(1/2)} \tag{3.8}$$

where δR is the total uncertainty and δx_1 to δx_n are the measurement uncertainties in x_1 to x_n. Executing the uncertainty analysis analytically can be a very demanding task due to the complexity of the data reduction procedure. However, the uncertainty analysis can be executed numerically using a method outlined by Moffat [43].

The data reduction program constructed in Matlab utilized the experimental data to determine the Reynolds number, friction factor and minor loss coefficient along with their associated uncertainties. In the uncertainty analysis, the data reduction program was first used to compute the values of $R_{i+\epsilon}$, e.g., *Re*, *f*, *K*, *V*, etc, for positively perturbed values of the measured variables x_i. These results were returned to the main program and combined with similar results for $R_{i-\varepsilon}$ obtained for negatively perturbed values of x_i. The values of $R_{i+\epsilon}$ and $R_{i-\varepsilon}$, the results for positively and negatively perturbed values of x_i,

were then used to determine the partial derivative (sensitivity coefficient), $\delta R/\delta x_i$, numerically using a central difference formulation,

$$\frac{\partial R}{\partial x_i} \approx \frac{R\left[x_1, x_2, \ldots.(x_i + \varepsilon_o), \ldots.x_n\right] - R\left[x_1, x_2, \ldots.(x_i - \varepsilon_o), \ldots.x_n\right]}{2\varepsilon_o} \tag{3.9}$$

where ε_o is the perturbation. The program then selected the measurement uncertainties to calculate the uncertainty in *Re*, *K*, *f*, etc. using equation 3.8. The measurement uncertainties associated with the data acquisition equipment are presented in Table 3.3. The results of experimental uncertainty will be discussed in Chapter 5.

Table 3.3: Summary of uncertainties of measured data

Measurement	Unit	Uncertainty
T_{in} and T_{out}	°C	0.1
Setra Pressure Sensor	psi	0.15% of full scale
Mass Balance	g	±0.01
Lab View Internal Clock	s	±0.01
Mass Flow Rate	kg/s	≈0.15%
Channel Length	μm	±1.0
Channel Width	μm	±1.0
Length Sample to Detector*	mm	±0.5
Traverse Distance of Fringes*	mm	±0.005
Angle of Incidence*	degrees	±0.0417

*Measurements required for depth measurement using laser interferometry

This chapter provides descriptions and explanations on how and why the experiment was designed and conducted. Significant information and guidelines regarding microchannel design, microchannel fabrication procedure, dimension characterizations and data reduction analysis are discussed. During the course of manufacturing microchannels in this study, it was experienced that xurography produces rough channel cut and often results in many other microchannel defects. Chapter 4 will discuss these microchannel defects in more detail.

CHAPTER 4

MICROCHANNEL DEFECTS AND SURFACE ROUGHNESS

Xurography has been used as a novel technology for manufacturing microfluidic channels. It is important to characterize the quality of the microchannels fabricated using this unique manufacturing technology. This chapter describes the methods, procedures and the results of surface roughness characterization and the microchannel defects that are associated with the xurographic manufacturing technology.

4.1 Introduction

In classical fluid mechanics, the friction factor is independent of wall roughness in laminar flow. However, in microscale flow, the surface phenomena such as hydrophobicity, hydrophilicity and surface roughness can become more significant [44].High surface roughness can cause inconvenient flow behaviors in the microchannels, e.g., decreasing the flow rate and creating bubbles from the liquid at the channel surfaces. In addition, several publications have proposed surface roughness as a possible source of error that caused microscale flow to deviate from Stokes flow theory [11, 20, 21]. Surface roughness and roughness features on the channel walls increase the shear stress, thus causing additional pressure drop for the flow. It has also been theorized that surface roughness may lead to early turbulent transition in microchannels.

The effects of surface roughness on the characteristics of flow in microchannels have been studied for the last two decades. Pfund et al. [21] performed an experimental

investigation of water flow in high aspect ratio microchannels with depth varying from 128 μm to 521 μm. The flow covered a *Re* range from 60 to 3450. The effects of surface roughness were investigated by introducing a rough bottom surface plate. The results indicated a strong possibility that the surface roughness caused the friction factor to increase in laminar flow. However, the authors also pointed out that there were large uncertainties in their experiment and a further investigation was suggested to confirm their results. Qu et al. [22] studied the surface roughness effects in silicon microchannels with relative roughness varying from 3.6% to 5.7%. Their results indicated that surface roughness is an important factor in characterizing fluid flow behaviors at the microscale. Additionally, early turbulent transition was found and was explained to be associated with the effect of surface roughness.

Wu et al. [45] conducted a systematic study on 13 silicon trapezoidal microchannels with two different channel heights of 56.22 and 110 μm. The relative roughness of the wall surface varied from 0.00326% to 1.09%. The friction factors were reported based on the pressure measurements at the inlet and outlet. The friction factors for the rough channels were found to be around 20% higher than those for lower roughness channels. The Poiseuille number increased over the theoretical values in the laminar regime. Kandlikar et al. [46] experimentally investigated the effects of surface roughness on heat transfer and fluid flow characteristics in small diameter tubes. Two stainless steel minichannels with diameters of 0.62 mm and 1.032 mm were tested. The surface roughness varied from 1.9 μm to 3.0 μm and the tests were conducted with water over the *Re* ranges of 900 to 3000 for the 0.62 mm tube and 500 to 2600 for the 1.032 mm tube. They reported that for the smaller diameter tube, an increase of surface

roughness generated higher pressure drops and an early turbulent transition. However, the larger diameter tube did not exhibit any roughness dependency over the experimental data range. Additionally, Kandlikar et al. recommended systematic studies on the roughness effect for microchannels where the surface roughness effects were expected to be higher.

The effect of surface roughness on turbulent flow transition is another topic that has been studied over the past few decades. A number of researchers, including Pfund et al. [21], Qu et al. [22] and Kandlikar et al. [46], reported that the effects of surface roughness evidently existed during the flow transition to turbulence. Kandlikar et al. [47] proposed the following equations to predict the flow transition to turbulence:

$$0 < \varepsilon / D_{h,cf} \leq 0.08 \qquad Re_{t,cf} = 2300 - 18{,}750\ (\varepsilon / D_{h,cf}) \tag{4.1}$$

$$0.08 < \varepsilon / D_{h,cf} \leq 0.015 \qquad Re_{t,cf} = 800 - 3270\ (\varepsilon / D_{h,cf} - 0.08) \tag{4.2}$$

where ε is the surface roughness, $D_{h,cf}$ is the hydraulic diameter based on constricted flow, and $Re_{t,cf}$ is the transition Reynolds number.

4.2 Methods and Procedures

To quantify the quality of the microchannels produced with the xurographic manufacturing technique, it is necessary to measure the surface roughness of the microchannel sidewalls. Due to ease of operation, an optical microscope was used for the initial examination of the surface roughness of channel sidewalls. Optical microscopy is an excellent tool to examine the sample surface before using other more advanced measurement tools. A 5 megapixel digital camera was connected to the microscope which allowed high quality top view images of the microchannels to be acquired. In order

to examine the surface of the channel sidewalls, the microchannel had to be oriented at a 45° angle such that the surface of channel sidewall is perpendicular to the emitted light from the microscope. However, due to the small working distance under an optical microscope, it was impossible to orient the microchannel at such an angle; thus, no channel sidewall images were acquired using an optical microscope.

Another attempt was made using a scanning electronic microscope, FEI Quanta 600 FEG SEM, to examine the channel sidewall surface and any possible defects in the microchannels. Some advantages of SEM are the large working space, high magnification and the capability of producing 3D images. However, due to the nature of SEM, it was incapable of acquiring images of the channel sidewalls with the top glass plates of the microchannels in place. To overcome this issue, four xurographic samples were fabricated without the top glass cover plates. The channel designs were cut on the Kapton® tape and the cut sections were then removed. The exposed surface of the tape was then bonded to the bottom glass plate. On the other side of the tape, the protective plastic film was removed and the sample was placed in the SEM machine for characterization. It should be noted that the samples were not cured, as described previously in the fabrication section. The sample was then tilted at an angle of 45° so that the channel sidewall was perpendicular to the scanning beams. The images of channel sidewall surfaces were successfully acquired and are presented in the result section of this chapter.

As discussed in Chapter 1, the surface roughness can be measured using a contact method (e.g., stylus profilometer) and a noncontact method (e.g., optical profilometer). The first attempt to measure surface roughness of the channel sidewalls was performed

using a stylus profilometer, Tencor P-20 in MicroFab laboratory at University of Utah. A stylus profilometer is an instrument that uses a diamond stylus to transverse across the sample surface and measure the roughness as a function of vertical position. Even though the Tencor P-20 has a stylus tip radius of 2 μm the stylus is tapered at a 60° angle making its shank diameter as large as 300 μm. Since the Kapton® tape has a thickness of approximately 105 μm, the Tencor P-20 stylus profilometer was incapable of measuring the surface roughness of the channel sidewalls.

Surface roughness of the microchannel sidewall was then determined using a Zygo optical profilometer in Surface Analysis laboratory at University of Utah. Roughness measurements of the actual tested microchannel assemblies could not be obtained due to sample size constraints of the profilometer. Therefore, a set of six smaller xurographic samples were fabricated in a method identical to the tested channels. A diamond saw was used to cut a glass plate into rectangular samples with dimensions of 50.8 mm x 8 mm x 3.2 mm. Two pieces of glass were bonded to both sides of cut Kapton® tape so that the cut edge of the tape was aligned with the edges of the glass plates. These samples were cured using the same conditions as those for the microchannels, as described previously. Forty transverse scans were made at intervals of 1.0 mm along the sample length; the arithmetic mean (R_a) and root-mean-square (R_{rms}) roughness were determined from the scan data.

4.3 Results and Discussion

4.3.1 Surface Roughness Using Zygo Optical Profilometer

Using the Zygo optical profilometer, the arithmetic mean and root mean squared roughness were measured across the microchannel sidewall surfaces. The mean values and standard deviations of R_a and R_{rms} surface roughness for the 40 scans for each sample were computed and are reported in Table 4.1. A sample of a surface roughness profile across a microchannel sidewall (sample #3) is presented in Figure 4.1.

Table 4.1: Roughness measurements of a xurographic test article across the sidewall surface.

Sample #	R_a (μm)	Std. Dev. (μm)	R_{rms} (μm)	Std. Dev. (μm)
1	1.598	0.349	2.022	0.289
2	1.676	0.323	2.136	0.320
3	1.601	0.283	2.069	0.298
4	1.615	0.234	2.077	0.227
5	1.577	0.192	1.899	0.227
6	1.583	0.186	2.052	0.237
Average	1.609	0.261	2.043	0.266

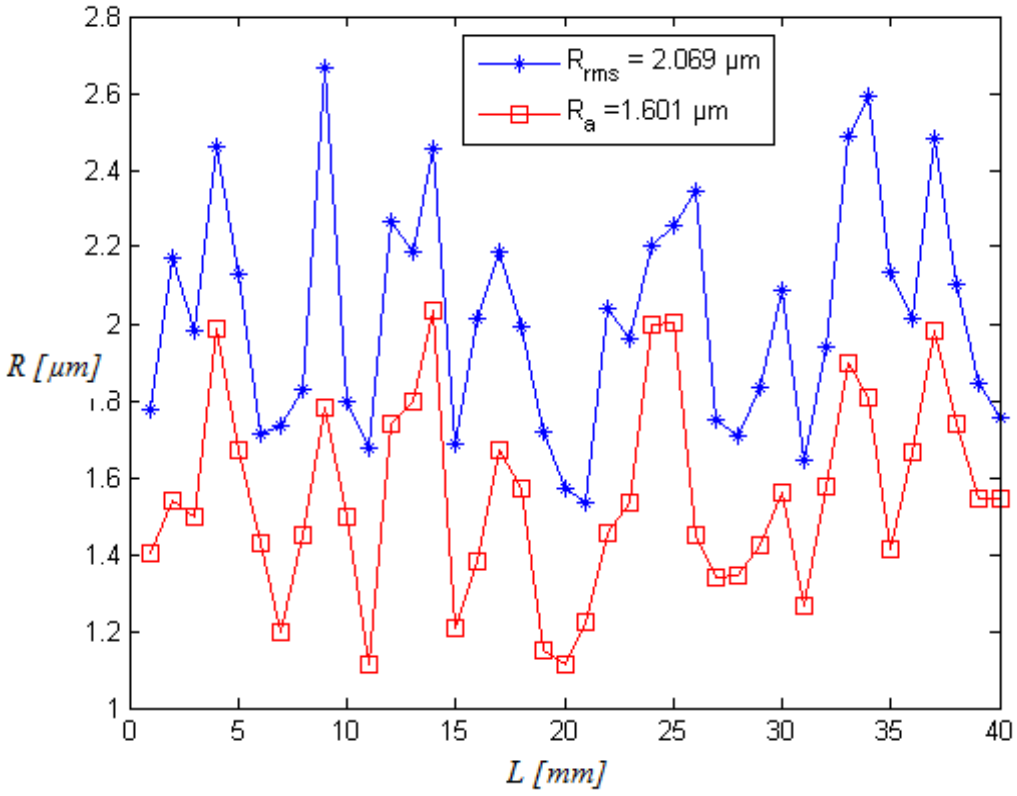

Figure 4.1: Surface roughness across a xurographic test article sidewall using a Zygo optical profilometer.

Figure 4.2 represents the sample images of xurographic test article sidewall surfaces that were characterized using a Zygo optical profilometer. The results in Fig. 4.2 represent typical surface roughness of the cut made with the cutting plotter. The images also revealed that the cut surface of the polyimide film was rougher than the two adhesive layers. This undesirable trait is most likely due to the different response the adhesive and polyimide film have to the cutting process. Furthermore, the cut surface roughness could be affected by the curing process of the Kapton® tape and glass plates as well as the nanoport curing process. Note that the latter curing process was not replicated in the fabrication of the test articles for the surface roughness characterization.

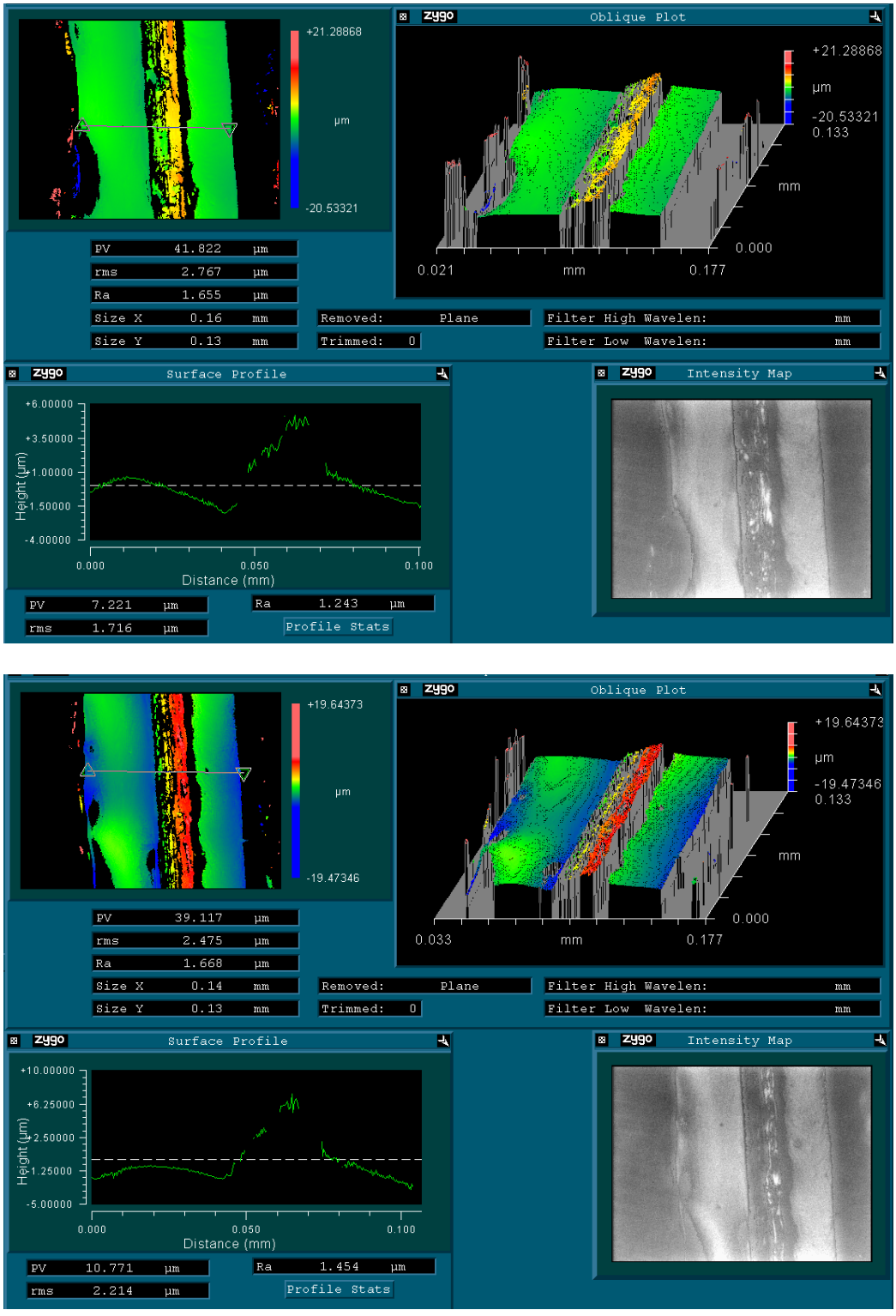

Figure 4.2: Sample images of xurographic test article sidewall surface during characterizations with a Zygo optical profilometer.

4.3.2 Microchannel Defects

The benefits of xurography include low costs and rapid production times; however, this technology is inferior to micromachined channels when precision is considered. Even though the Graphtec plotter has a resolution of 10 μm, this precision was not achieved. Observation of cut microchannels was using a scanning electronic microscope and an optical microscope; the results are shown in Figs. 4.3, 4.4, 4.5 and 4.6.

Post cut observation under an optical microscope using 10x magnification indicated that the cutting and tape removal processes produced rough cuts, especially at abrupt features, e.g., pressure taps and miter bend corners. During the cutting process, the blade had a tendency to drag small portions of adhesive at abrupt features, as shown in Fig. 4.3a. As the adhesive attached to the blade, it produced a rough cut along the channel length. Furthermore, a portion of the adhesive attached to the blade could detach and subsequently reattach to the channel wall, as exhibited in Fig. 4.3b. In many cases, this adhesive droplet appears to constrict the channel width, though it is unclear if any of the extending adhesive or droplets spanned the height of the channel or attached to one of the glass surfaces only.

Observations with an optical microscope using 20x magnification, and with an SEM, also revealed that the channel wall was rough and wavy, as shown in Figs. 4.3c, d and Figs. 4.4 a, c, d, and e. This result was also observed during a characterization with an optical profilometer. The cut surface of the polyimide film was found to be rougher than the two adhesive layers. Additionally, evidence of either the polyimide film expansion or adhesive layer contraction was observed in several microchannels, as shown

in Fig.4.4f and Figs 4.5a, b. This undesired trait could be associated with the curing process of the Kapton® tape and two glass plates.

Another defect was attributed to uncut adhesive left inside the microchannel at corners. Since the cutting blade had a 45° edge, the blade had a tendency to undercut the tape at the 270° inner wall of the miter bend (as shown in Fig. 4.3e), where the angle is defined between the surfaces forming the microchannel miter bend. Thus, a small portion of uncut adhesive often remained inside the channel at abrupt corners. This effect was dependent on the plotted cutting direction, which can result in unsymmetrical corners in a contraction/expansion feature (see Figs. 4.6a, b, c, d, e and f). On the other hand, the blade tended to overcut the tape at the 90° outer wall angle in the miter bend, resulting in material protrusions into the microchannel, as shown in Fig 4.3f, Figs. 4.4a, b, c, d, e and Figs. 4.5c, d, e, f.

When the blade cut abrupt features, it was capable of abruptly swiveling and turning; however, as the blade swiveled in the adhesive, a small tear in the film could be created. This defect often occurred when the abrupt corners were closely spaced. In addition, as the blade swiveled and turned, it often pulled on the cut corner causing the channel to widen or contract. Width measurements indicated that the plotter produced more precise cuts at large dimensions ($W > 600$ μm) than at the smaller ones ($W < 300$ μm).

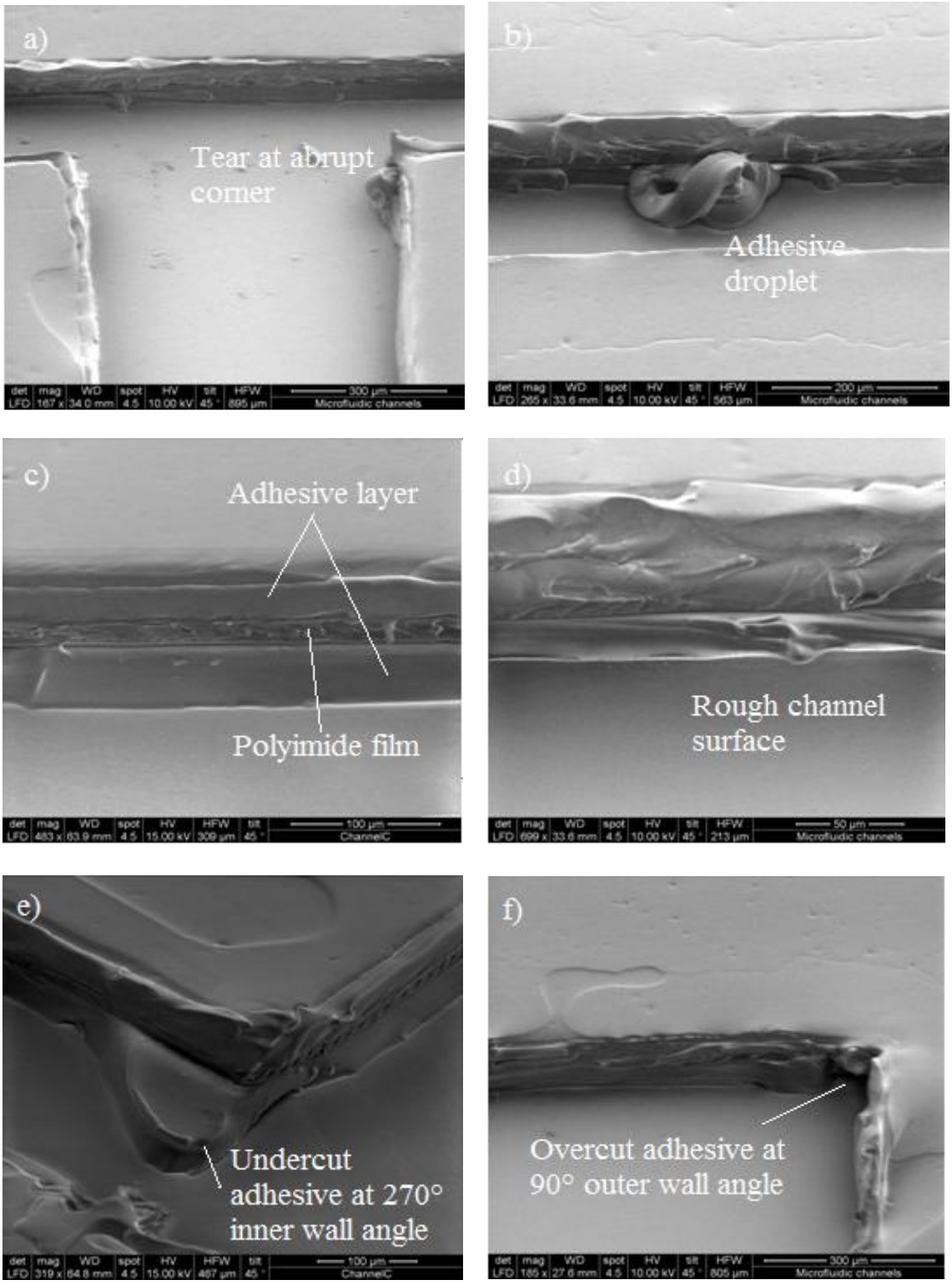

Figure 4.3: SEM images of xurographic microchannel defects.

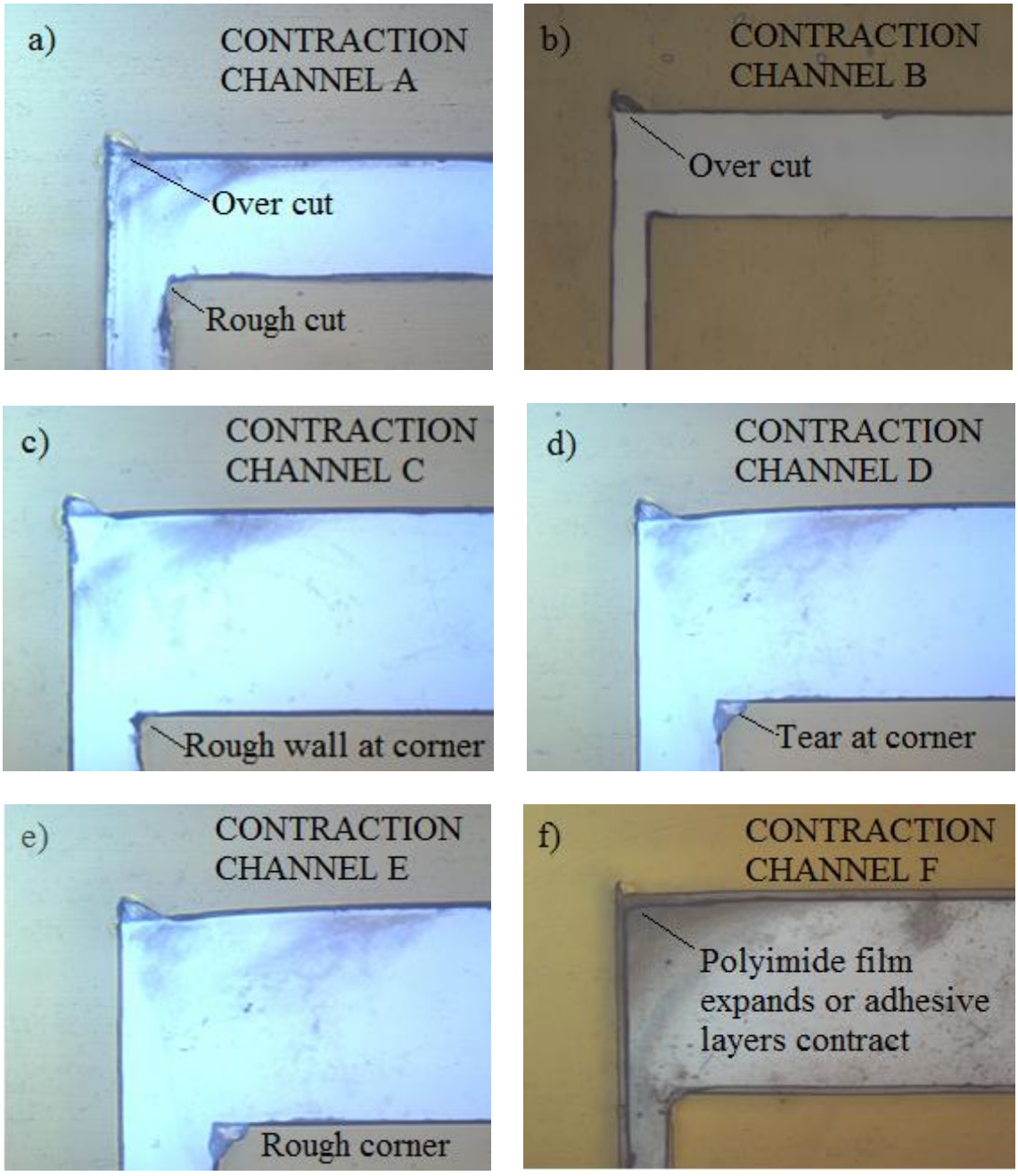

Figure 4.4: Sample images of six contraction microchannels at 90° miter bend. Flow direction is into contraction section.

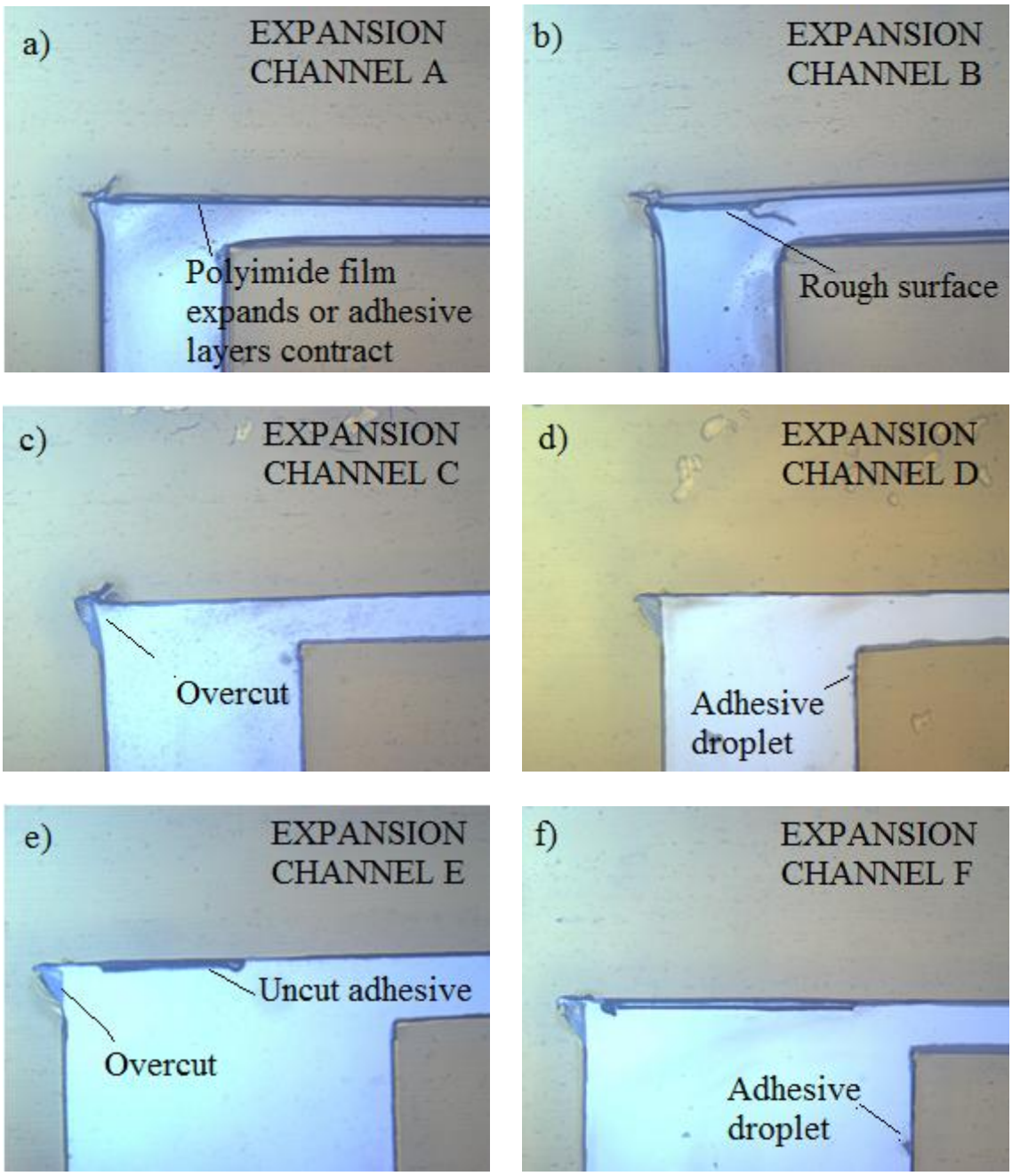

Figure 4.5: Sample images of six expansion micochannels at 90° miter bend. Flow direction is into expansion section. The images were taken using an optical microscope.

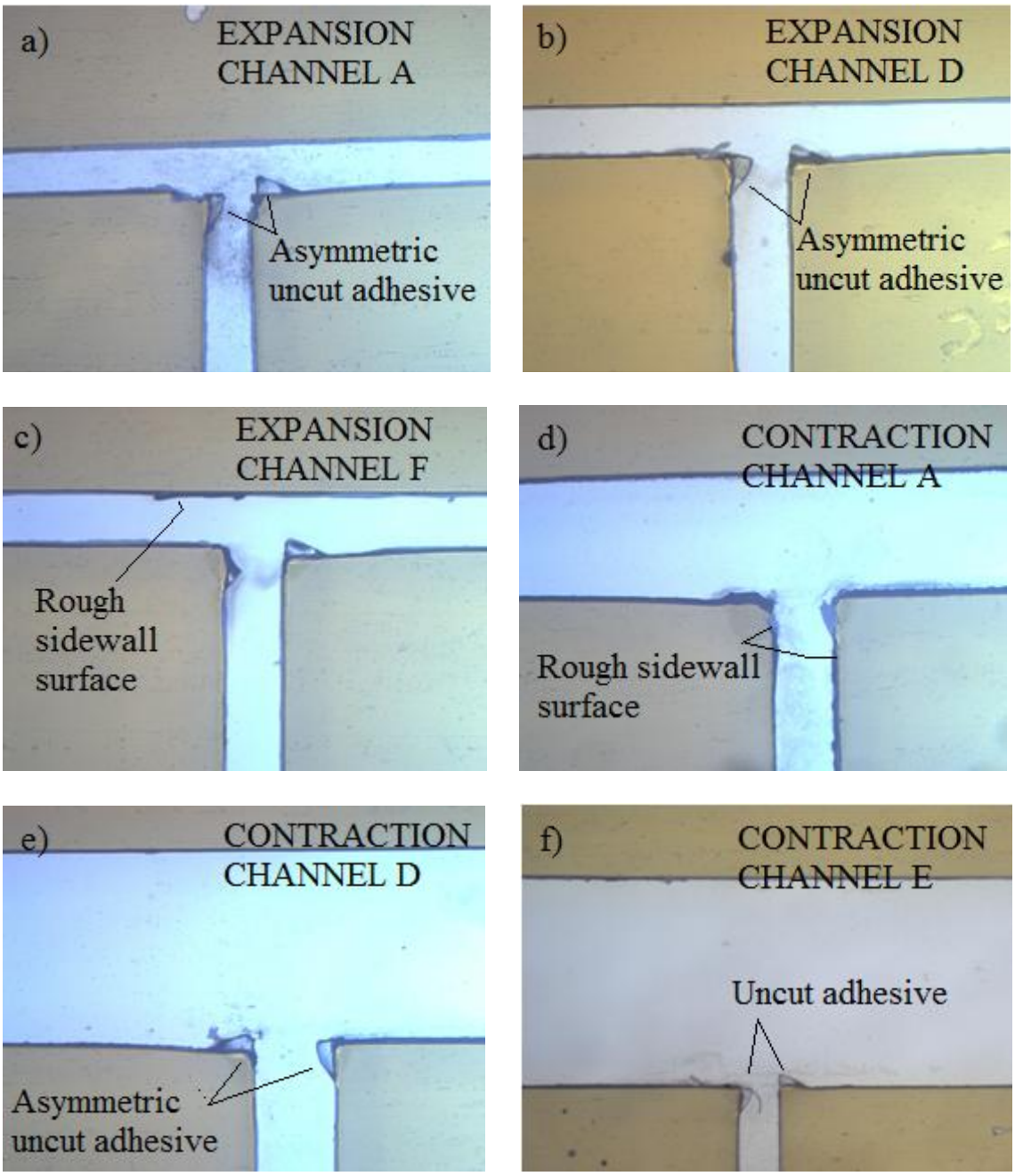

Figure 4.6: Sample images of xurographic channel walls at the pressure taps.

4.4 Recommendations for Minimizing Microchannel Defects

During the course of this project, many attempts were made to produce cleanly cut channels. On occasion, after the channel was cut and observed under a microscope, the channel was discarded because of its poor quality as evidenced by rough cuts and/or uncut adhesive at pressure taps or 90°corners. When this occurred, the process was started again until a clean cut channel was obtained. Usually, no more than three or four attempts were required to produce an acceptably cut channel with a sharp cutting blade.

The imprecise cuts obtained at abrupt corners were an unfortunate characteristic of the xurographic manufacturing process. Several procedures were found to minimize the aforementioned defects:

- The cutting plotter environment must be clean. This reduces the possibility of dust, hair and any other particles being attached to the adhesive layer.
- The Kapton® tape should be laid flat and in alignment with the two rollers when inserted into the cutting plotter. Non straight channel cuts can be produced if the tape is not flat.
- The cutting blade must be sharp and clean. A dull blade results in a very rough cut and other undesirable features.
- The cutting speed of the plotter must be set at its lowest setting. High cutting rate may result in a rough cut and inaccurate dimensions.
- The cutting force should be set to 30% of its maximum. Very low cutting force results in under-cutting of the tape. High cutting force results in an over-cut of the tape and may damage the cutting blade.

- Great care must be exercised during the removal of the cut tape. The cut tape should be removed at the square reservoir initially, followed by further tape removal in the straight channel sections. This process reduces the damage that a tweezer can cause on the channel wall.
- While the cut Kapton® tape is viewed under a microscope, a tweezer with a very fine point can be used to remove pieces of uncut tape and noticeable adhesive from the microchannels.
- The glass surface must be clean before bonding to the adhesive layer. This will reduce the possibility of dust and other particles being introduced to the channels.
- The Kapton® tape microchannels must be cured at an appropriate temperature as discussed in Chapter 3. Over curing the tape may result in a rough channel wall.

CHAPTER 5

RESULTS AND DISCUSSION

Twelve microchannels were tested: six 90° bends with an expansion and six 90° bends with a contraction. The friction factor, Poiseuille number, critical Reynolds number and minor loss coefficient associated with the 90° miter bends are reported and discussed in this section. Note that the upstream Reynolds number is used in all data presentations.

5.1 Frictional Pressure Loss

The experimental friction factor data, f_{exp}, along with f_{thry} obtained from equation (3.5) for the microchannels containing expansions and contractions at the 90° miter bends are shown in Figs. 5.1 and 5.2, respectively. All the microchannels containing an expansion after the bend were designed with the same entrance geometry; therefore, only one theoretical friction factor for one aspect ratio is presented in Fig. 5.1. Due to plotter imprecision, the entrance aspect ratio of all microchannels presented in Fig. 5.1 deviated from their nominal designed values, causing f_{exp} to deviate slightly from the expected theoretical correlation. Similarly, three theoretical friction factors for the different aspect ratios are presented in Fig. 5.2 for the entrance section of the contraction microchannels.

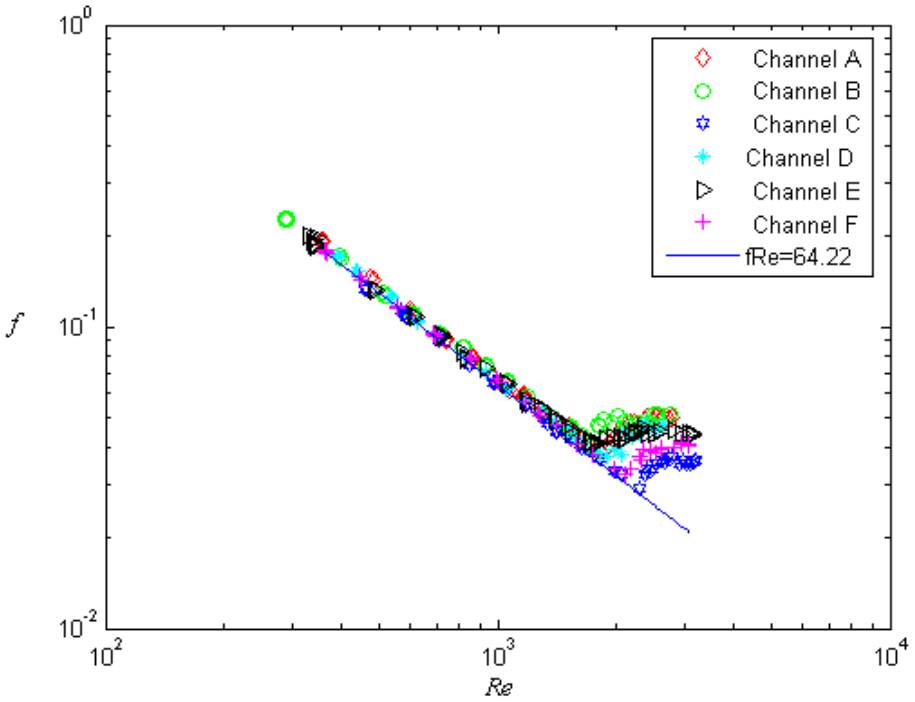

Figure 5.1: Experimental and theoretical friction factor for the entrance section of all microchannels containing an expansion at the bend.

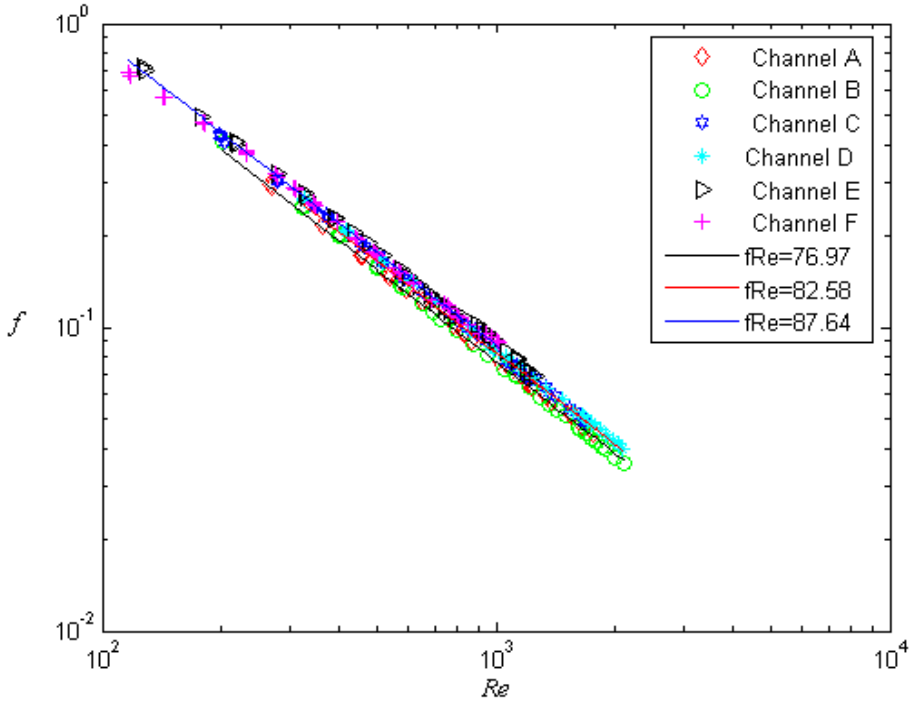

Figure 5.2: Experimental and theoretical friction factor for the entrance section of all microchannels containing a contraction at the bend.

Relative uncertainty for the experimental friction factor, δf_{exp}, was influenced significantly by the uncertainty of the pressure and depth measurements, especially at low *Re*. The uncertainty of f_{exp} ranges from 9.5% to 2.3% in all bended microchannels containing an expansion. The highest uncertainty occurred at the lowest *Re*. δf_{exp} was as high as 9.5% for $Re < 350$, but decreased to less than 3.5% for $Re > 1000$ and further decreased to less than 2.3% for $Re > 2800$. Similarly, δf_{exp} ranges from 31% to 2.8% for all bended microchannels containing a contraction. δf_{exp} was significantly higher for contractions in comparison to expansions due to ΔP_{23} being relatively small. For microchannels A, B, C, and D containing a contraction, δf_{exp} was as high as 16.5% for $Re < 200$, but decreased to less than 7% for $Re > 500$, and was less than 3.5% for $Re > 1000$. For microchannels E and F containing a contraction, δf_{exp} was as high as 31% for $Re < 150$ and decreased to less than 8.4% for $Re > 400$ and was less than 5.6% for $Re > 1000$. Due to the low pressure drop between pressure taps 1 and 2, δf_{exp} for channels E and F was higher than channels A, B, C, and D. The relative uncertainty for *Re* was less than 0.67% for all data sets.

5.2 Critical Reynolds Number Range

Table 5.1 and 5.2 present the theoretical and experimental Poiseuille numbers in the laminar flow regime for all microchannels. The ratio of Po_{exp} to Po_{thry} is also presented in Fig. 5.3 and 5.4, where Po_{thry} is only valid for laminar flow. Note that this ratio equals unity when the flow follows macroscale laminar theory. The data are shown for the entrance section of all bended microchannels. Channels A and B containing an expansion have the highest percentage difference between Po_{exp} and Po_{thry}, which is

Table 5.1: Comparison of theoretical and experimental *Po* in laminar flow and Re_{cr} in the upstream straight sections of all 90° miter bend microchannels containing an expansion.

Channel	$\alpha_{entrance}$	Po_{thry}	$Po_{exp,avg}$	% Diff.	Re_{cr} *Range*
A	0.429	64.44	68.48	6.27	1,692 - 1,815
B	0.400	65.51	71.87	9.71	1,746 - 1,819
C	0.434	64.27	65.93	2.58	2,244 - 2,338
D	0.420	64.76	67.98	4.97	1,809 – 1,984
E	0.395	65.70	67.94	3.41	1,778 - 1,872
F	0.435	64.23	66.45	3.34	2,103 - 2,178

Table 5.2: Comparison of theoretical and experimental *Po* in laminar flow and Re_{cr} in the upstream straight sections of all 90° miter bend microchannels containing a contraction.

Channel	$\alpha_{entrance}$	Po_{thry}	$Po_{exp,avg}$	% Diff.	Re_{cr} *Range*
A	0.189	77.01	80.38	4.38	--
B	0.191	76.94	78.67	2.24	--
C	0.115	83.28	85.96	3.22	--
D	0.123	82.54	85.26	3.30	--
E	0.071	87.64	90.35	3.10	--
F	0.071	87.64	89.81	2.48	--

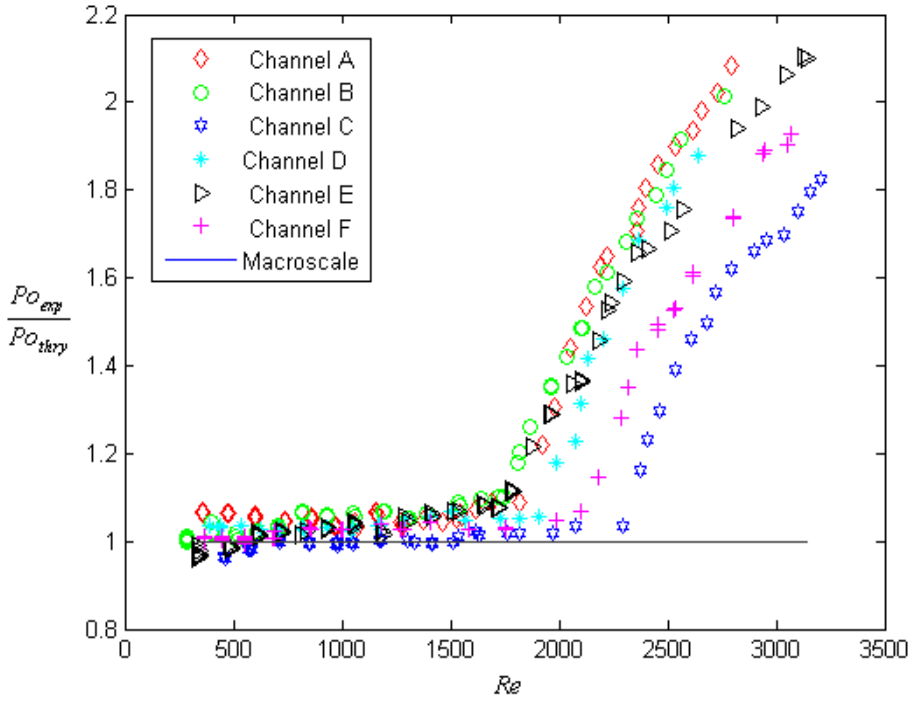

Figure 5.3: Ratio of experimental *Po* to theoretical *Po* for the entrance section of all microchannels containing an expansion at the bend.

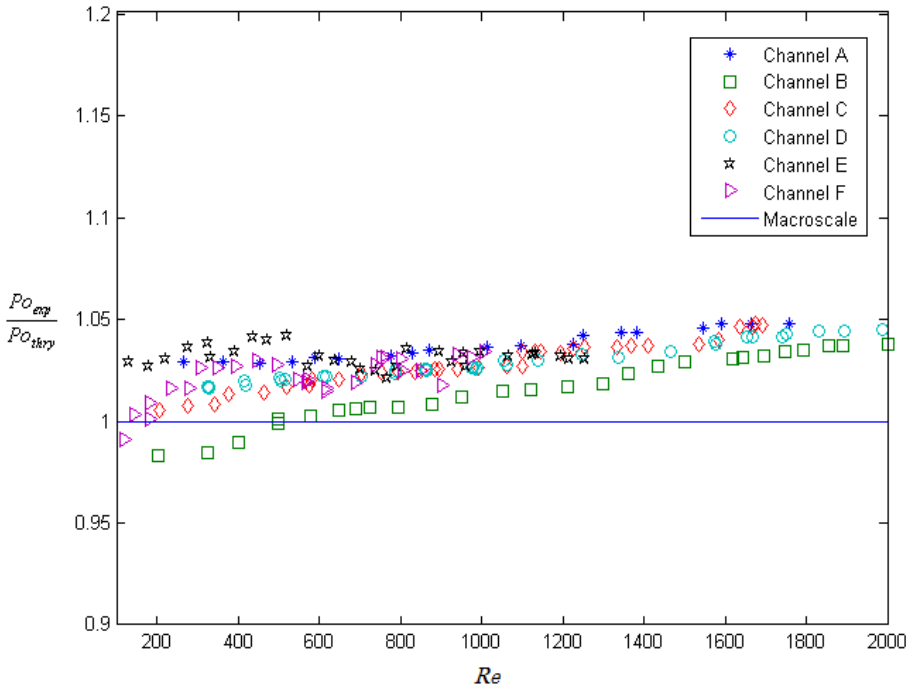

Figure 5.4: Ratio of experimental *Po* to theoretical *Po* for the entrance section of all microchannels containing a contraction at the bend.

approximately 7.0% and 10.0% for the two channels, respectively. The bended microchannels containing an expansion have a higher percentage difference in experimental and theoretical Poiseuille numbers in comparison to all bended microchannels containing a contraction. The percentage difference in Po_{exp} and Po_{thry} is less than 4.4% for all bended microchannels containing a contraction. The differences in performance for the microchannels containing an expansion or contraction may be due to the fact that the microchannels defects such as a roughness, adhesive droplets and uncut adhesive at the corners and pressure taps have a greater effect on the flow behavior in microchannels that have smaller hydraulic diameters. Another more pragmatic explanation is that all the contraction microchannel tests were performed after those for the expansion channels. As the fabrication method evolved over time and lessons were learned on how to create better microchannels, fewer defects were produced in the channels containing contractions. However, the experimental and theoretical Poiseuille numbers are overall in good agreement for laminar flow, with a maximum difference of approximately 10% for the microchannels containing an expansion.

The Reynolds number range for laminar flow corresponds to the linear region of the f_{exp} (Re) data on *log-log* coordinates, as shown in Figs. 5.1 and 5.2. Similarly, Re_{cr} is identified as the Re value where f deviates from this linear relation for increasing Re. Using the aforementioned criteria, Re_{cr} for the straight entrance sections ranges from 1700 to 2300 for all bended microchannels containing expansions, as reported in Table 5.1. Due to the low range of Re in the bended microchannels containing contractions, the critical Reynolds number range could not be determined for these microchannels. Early flow transition (low Re_{cr}) in xurographic microchannels is believed to be associated with

defects introduced by the manufacturing process. These defects include wavy channel walls, adhesive droplet attachment on the glass surface, and uncut adhesive at abrupt corners. In addition, due to the possible uneven application of clamping torque, the depth of microchannels varies slightly (as discussed in the microchannel depth characterization section), potentially causing the flow to transition at low Re_{cr}. It should be noted that even with these defects, Re_{cr} is in good agreement with data in the literature [7, 25, 27].

5.3 Minor Loss Coefficients

The minor loss coefficient data for microchannels with expansions are shown in Fig. 5.5. K_e data are reported for laminar and turbulent flow. K_e decreases rapidly with increasing Re for $Re \leq Re_{cr}$. K_e decreases at transition and remains nearly constant for $Re > Re_{cr}$. The discontinuity in K_e data in the transition regime is due to the abrupt change in β. In reality, β asymptotes from approximately 2 (for these channels) to 1 since the velocity profiles gradually flatten through transition with increasing Re. Considering all bended microchannels containing an expansion at low Re flows, the high magnitude of K indicate the large effects that the expansion has on the low energy flows. However, this expansion effect on the loss coefficients decreases as the flows approach higher Reynolds numbers.

Comparing the results of the present study to the data reported by Xiong and Chung [18], Costaschuk et al. [23] and Torgerson et al. [41], the decreasing trend in K_e with Re was also observed. The range of K_e data correlates well with the data reported by Torgerson et al. However, the magnitude of K_e data is slightly higher than the data

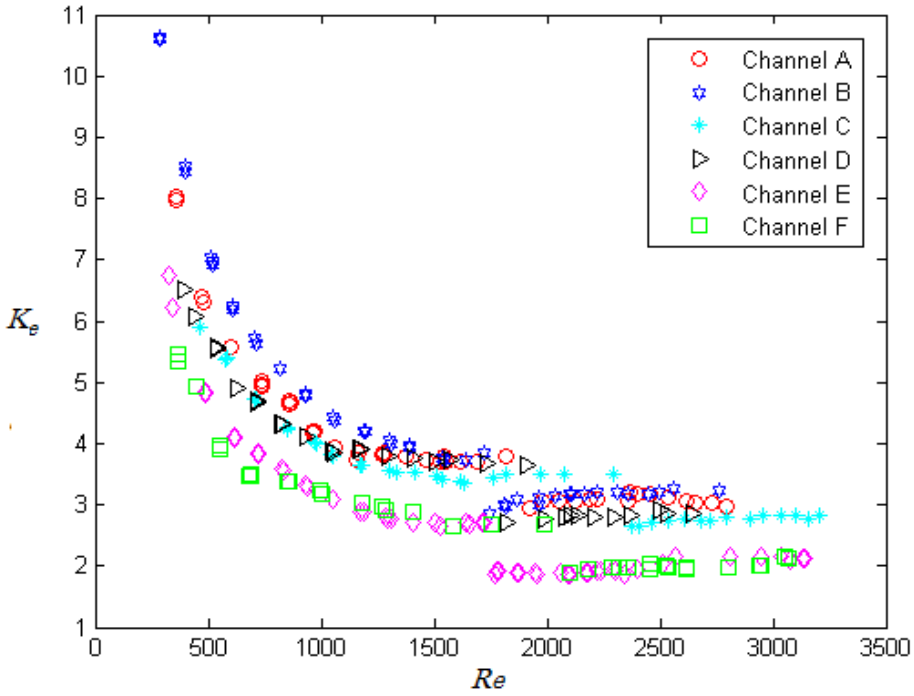

Figure 5.5: Minor loss coefficient data for all 90° miter bend microchannels containing an expansion.

reported by Costaschuk et al. Note that high precision and smooth microchannels were used in their study. Furthermore, near the critical Reynolds number the change in K_e decreases and is followed by an abrupt drop posttransition, which correlates with the data reported by Costaschuk et al. [23] and Abdellal et al. [35].

In addition, K_e decreases with decreasing area ratio, A_R, which is defined for an expansion as the ratio of channel cross-sectional area before and after the bend, i.e., $A_R < 1$. For low *Re*, the expansion and bend effect are the dominant mechanism compared to the kinetic energy since the loss associated with the expansion accounts for approximately 50 to 85% of the minor loss coefficient. However, for high *Re*, the effects

of kinetic energy dissipation on K_e become more important as the terms with the kinetic energy coefficients account for approximately 35 to 50% of the minor loss coefficient. The relative uncertainty in K_e for microchannels containing expansions ranges from as high as 12.5% for $Re < 400$ to less than 5.0% for $Re > 1000$.

The variation of K_c with Re for the bended microchannels containing a contraction is shown in Fig. 5.6, where A_R is the ratio of the area after the bend to the area before the bend, i.e., $A_R < 1$. K_c data were only obtained for laminar flow due to limitations on the available pressure sensors and channel failures at high pressures. The relative uncertainty in K_c ranged from 12.0% for $Re > 200$ to less than 3.8% for $Re > 500$. K_c gradually decreases with increasing Re. The high magnitude in K_c data at low Re indicates the significant effect that a contraction has on the low energy flows; however, as Re increases, this effect decreases. Furthermore, the minor loss coefficient data decrease with decreasing area ratio in 90° miter bends with a contraction.

The decreasing trend in K_c with Re was also observed in the data reported by Costaschuk et al. [23], Torgerson [28] and Zho et al. [34]. Note that microchannels with similar dimensions and rectangular cross sectional areas were studied by Torgerson and Costaschuk et al. while Zho et al. performed their study in circular microtubes with larger diameters. The magnitude of K_c for all six microchannels was slightly higher than reported by Costaschuk et al. and Zho et al. The discrepancy is most likely associated with xurographic micromanufacturing defects. The rough channel walls and remaining uncut adhesive at the 90° bend introduced additional unintended losses in the flow, resulting in a higher K_c.

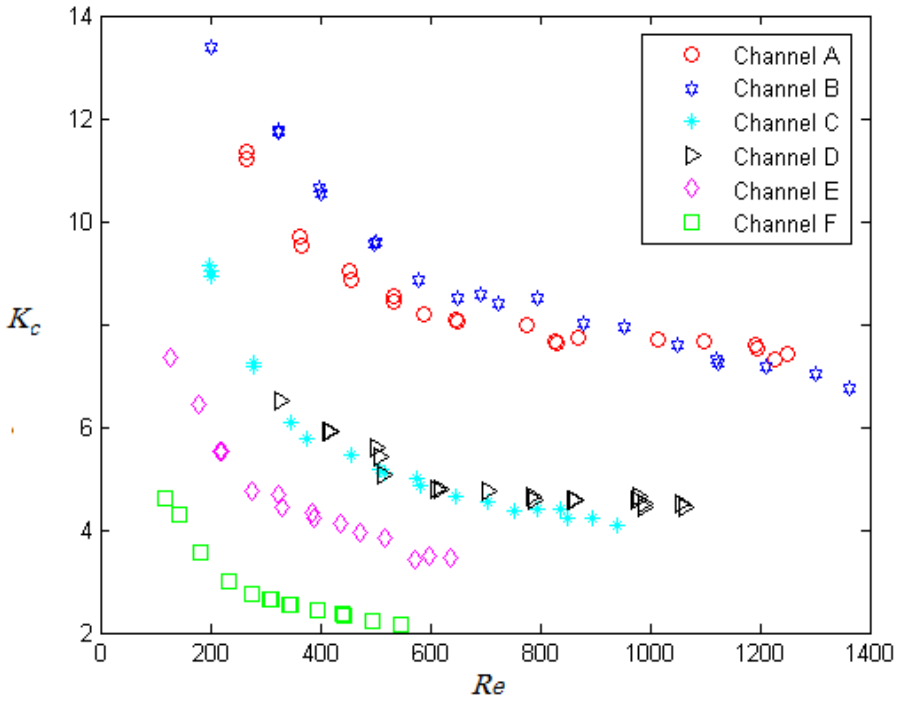

Figure 5.6: Minor loss coefficient data for all 90° miter bend microchannels containing a contraction.

The decreasing trend of $K_c$and K_e with increasing *Re* in 90° miter bends is similar to the trend of *K* data for straight flow through expansions and contractions reported by Torgerson et al. [41]. For the present study, *K* ranges from 2.0 to 11.2 and from 2.2 to 13.4 for all bended channels containing expansions and contractions, respectively. For the Torgerson et al. [41] study, the approximate *K* ranges are from 0.4 to 8.5 and from 18 to 61 for all channels containing expansions and contractions (no bends), respectively. However, the Torgerson et al. [41] contraction data were normalized by the upstream specific kinetic energy and the minor loss coefficient data for both contractions and expansions did not include the kinetic energy coefficients. The magnitude and trend of K_c and K_e data in 90° miter bends do not agree with the *K* data through 90° miter bends reported by Torgerson et al. [41]. The Torgerson et al. microchannels were designed

such that A_R = 1.0; however, due to cutting plotter imprecision A_R ranged from 0.73 to 1.0. In contrast, A_R ranged from 0.16 to 0.50 in the present study. Comparing the minor loss coefficient data reported by Torgerson et al. [41] to that of the present study suggests that the contraction/expansion effect is the dominant mechanism for minor losses in 90° miter bend for $A_R < 0.5$.

To combine the effects of *Re* and A_R on the minor loss coefficient, the K_e and K_c data were curve-fit as a function of A_R and *Re*. The assumed functional form was $K = CRe^m A_R^n$, where *C, m* and *n* are constants, which were determined using the multiple linear regression tool in Matlab. The *K* data were also normalized using a trial and error approach to collapse the data to a single curve. It was determined that if the *K* data were normalized by ReA_R^n, where *n* was obtained from multiple linear regression, the normalized data, K^*, collapsed to a single curve. The K^* data were then curve-fit assuming a power law relationship. The resulting curve-fits as a function of *Re* are presented as equations (5.1) and (5.2),

$$K_e^* = \frac{K_e}{ReA_R^{0.391}} = 220.8Re^{-1.513} \tag{5.1}$$

$$K_c^* = \frac{K_c}{ReA_R^{1.245}} = 291.44Re^{-1.431} \tag{5.2}$$

The variation of K^* as a function of *Re* in 90° miter bends containing an expansion or contraction are presented in Figs. 5.7 and 5.8, respectively. The correlations given in equations (5.1) and (5.2) for the normalized loss coefficients are presented along with the experimental *K* data for direct comparison in Figs. 5.9 and 5.10. These figures indicate that the correlations for K_c^* and K_e^* represent the experimental data trends well.

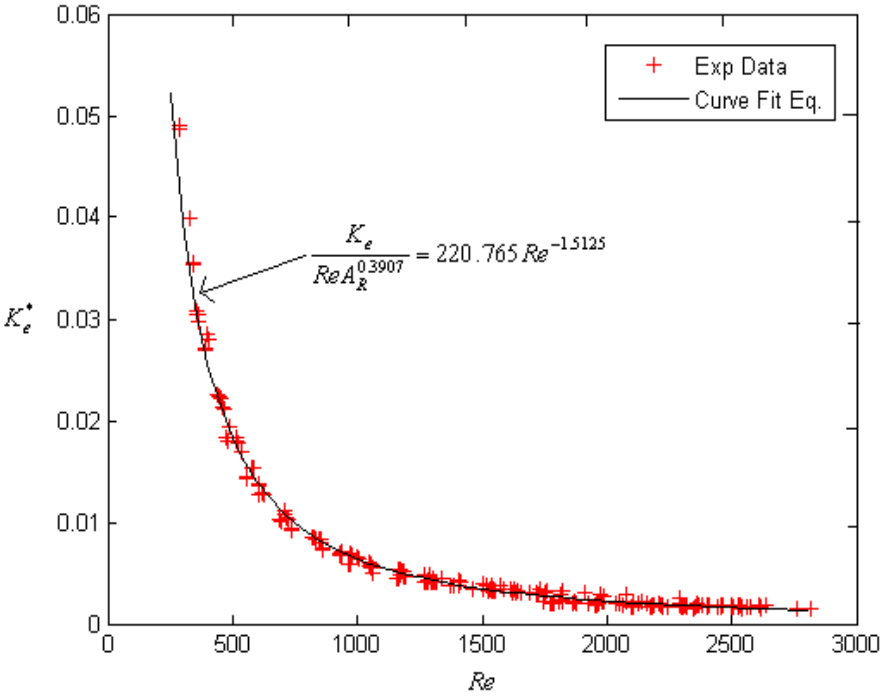

Figure 5.7: Normalized minor loss data for 90° miter bends with an expansion

.

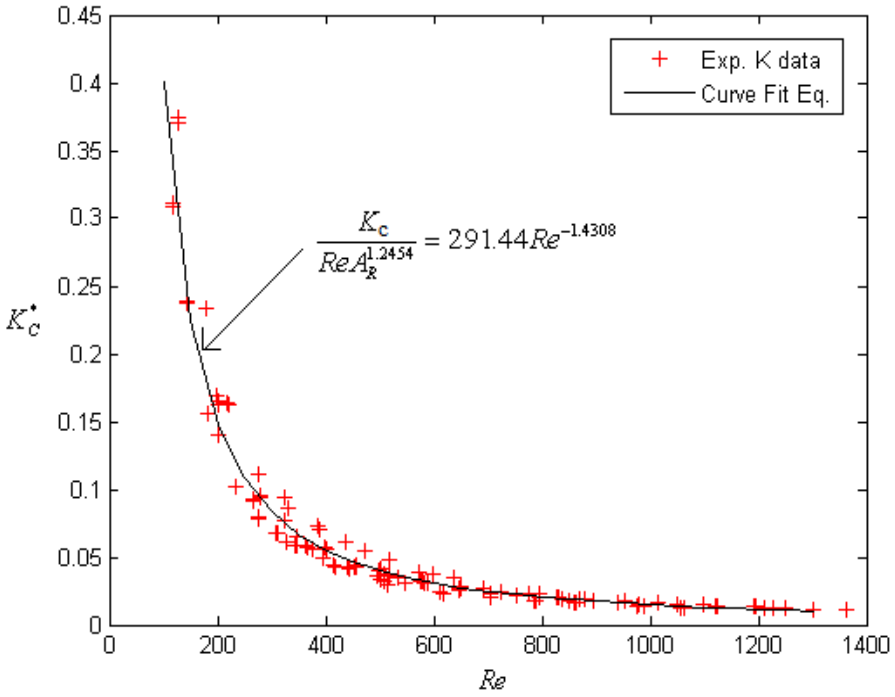

Figure 5.8: Normalized minor loss data for 90° miter bends with a contraction.

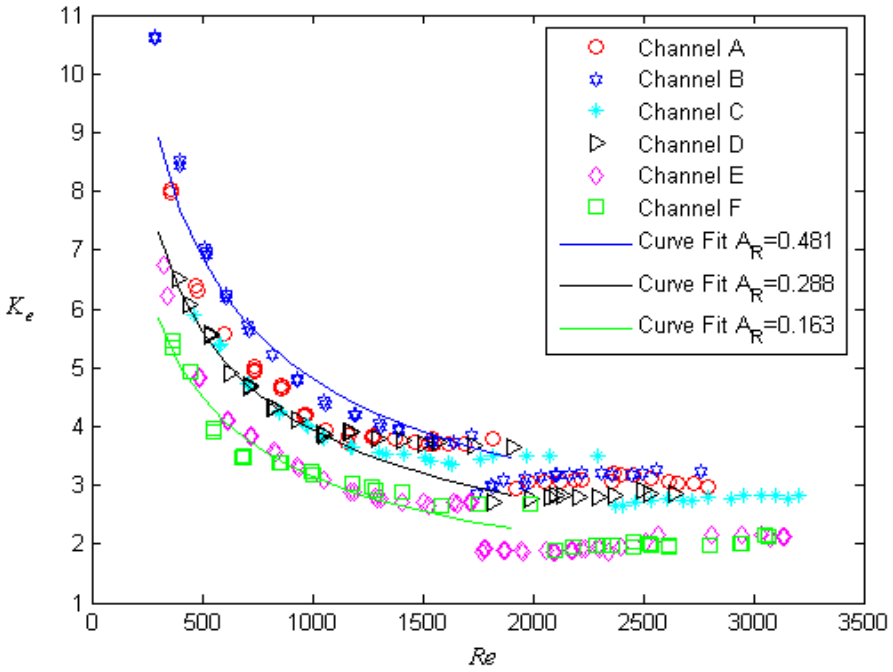

Figure 5.9: Minor loss coefficient data for 90° miter bends containing an expansion. Curve fit with area ratio of 0.481, 0.288, and 0.163 corresponding to channels B, D, and F, respectively. *C*, *m*, and *n* are 220.765, -0.5125 and 0.3907, respectively.

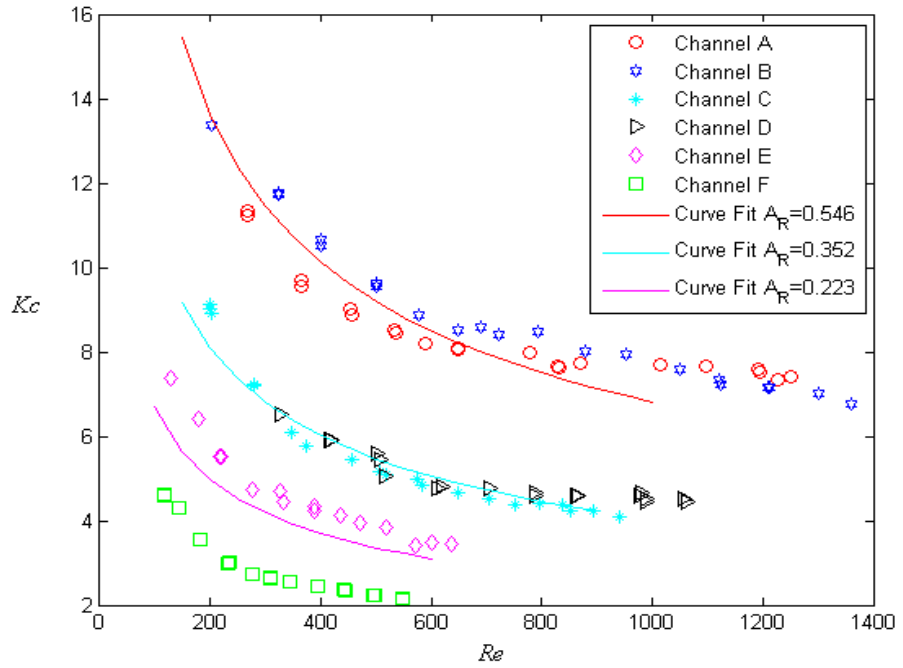

Figure 5.10: Minor loss coefficient data for 90° miter bends containing a contraction. Curve fits with area ratio of 0.546, 0.352, and 0.223 correspond to channels A, C, and E, respectively. *C*, *m* and *n* are 291.44, -0.4082 and 1.2454, respectively.

5.4 Summary

An experimental study of water flow in rectangular xurographic microchannels was undertaken to determine the minor losses for 90° miter bends that incorporate either a contraction or expansion. Friction factor data in the straight entrance sections were determined from the pressure drop between two pressure taps.

Even though the xurographic manufacturing process does not produce perfect channels, the frictional flow characteristics are in very good agreement with laminar flow theory. The critical Reynolds number was found to be in the range of 1700 to 2300, which is in general agreement with data in the literature. Early flow transition was attributed to xurographic manufacturing defects. Minor loss coefficient data in 90° miter bends with expansion decrease rapidly for $Re < Re_{cr}$. At transition, K_e drops and approaches an asymptotic value for $Re > Re_{cr}$. Loss coefficients in 90° miter bends with contractions were found to gradually decrease with Re. The magnitude of K_c in these microchannels was found to be higher than reported data found in the literature. This discrepancy was attributed to the rough cut channels and uncut adhesive remaining at abrupt corners in the bend, causing additional unintended losses. In addition, the minor loss coefficients decrease with decreasing area ratio through the contraction or expansion. The minor loss coefficient data were found to have the following general characteristics: (1) K is larger in the laminar region than in turbulent region, (2) K is dependent on both Re and the cross-sectional area ratio associated with the contraction or expansion in the 90° miter bends, and (3) the contraction/expansion effects are the dominant mechanism for losses in 90° miter bends with $A_R < 0.5$.

CHAPTER 6

CONCLUSIONS AND RECOMMENDATIONS

6.1 Conclusions

An experimental study was conducted to analyze the flow behaviors of distilled water in rectangular xurographic microchannels. The microchannels incorporating 90° miter bends with either a contraction or expansion were designed to determine the loss coefficient for these transitions. The frictional pressure drop and critical Reynolds number in the upstream straight sections were also determined to examine the validity of Navier-Stoke flow theory at the microscale level. The microchannels were fabricated using xurography. Kapton® tape with approximately 105 μm thickness was cut using a cutting plotter; the cut section was then removed. The remaining tape was sandwiched between two glass plates, forming a microchannel. A set of twelve microchannels were fabricated with hydraulic diameters ranging from 144.37 μm to 196.55 μm. The variations of hydraulic diameter were determined by changing the channel width as the channel depth was fixed by the thickness of the Kapton® tape.

Xurography is a relatively new rapid prototyping technique that has been used in biomedical and microfluidic applications. Xurography allows short fabrication time, does not require clean room technologies, and equipment and material costs are low compared to other rapid prototyping techniques. These advantages for xurography make it an ideal tool for the development of microfluidic systems in the laboratory. Unfortunately, this technology is inferior to micromachined channels when precision is considered. The

microchannels produced by xurography contain rough cuts and imprecise features. At 90° miter bends, the cutting blade is required to change cutting direction which causes undesired cut features. Several other defects in these xurographic microchannels include unremoved adhesive along the channel wall, over-cutting at 90° outer wall corners resulting in material protrusion into the microchannel, and under-cutting at 270° inner wall corners resulting in uncut adhesive remaining inside the microchannel. In addition, the arithmetic mean (R_a) and root-mean-square (R_{rms}) roughness of xurographic microchannel sidewalls were also characterized. The microchannel sidewalls had an average R_a and R_{rms} of 1.609 μm and 2.043 μm with standard deviations of 0.261 μm and 0.266 μm, respectively.

Microchannel characterization was emphasized to minimize the relative uncertainty of the reported results. The microchannels were characterized using nondestructive methods under conditions representative of the experiments. Channel length and depth measurements were made using a Nikon V12A profile projector that has a low measurement uncertainty of ±1.0 μm. Additional mechanical force was applied to the microchannels using a mechanical clamping system when the depth measurements were being made; the torque applied on each bolt was the same as that used in the actual flow experiments. The depth measurements were made using laser interferometry, which has relative uncertainty as low as 0.2%.

The frictional effects in the rectangular xurographic microchannels were characterized in the upstream straight sections in the form of friction factor, Poissuille number and critical Reynolds numbers. Turbulent data are available for the microchannels containing an expansion; however, due to pressure sensor limits, only

laminar data are available for the microchannels containing a contraction. From the results, there is no significant deviation from macroscale theory for friction factor due to microscale effects. The friction factor data were in agreement with macroscale theory within ±10%. The Poissuille number was found to be dependent on microchannel aspect ratio and correlated well with the macroscale correlations for laminar flow. The critical Reynolds number ranged from 1700 to 2300. Early turbulent transition was observed in these xurographic microchannels. This early transition is believed to be associated with the microchannel defects such as adhesive droplets on the channel wall and uncut adhesive at the corners and pressure taps.

Minor loss coefficients were determined for all 90° miter bend microchannels that contained either an expansion or a contraction. Loss coefficients through 90° miter bends with expansion decrease rapidly for $Re < Re_{cr}$. At transition, the loss coefficient suddenly drops and approaches an asymptotic value for $Re > Re_{cr}$. The discontinuity in K_e data in the transition regime is due to the abrupt change in kinetic energy coefficient β. For 90° miter bends with contractions, loss coefficients gradually decrease with increasing Re for $150 < Re < 1400$. The K_c data are slightly higher than the data reported in the literature. This discrepancy was attributed to the rough cut channels and uncut adhesive remaining at abrupt corners in the bends, causing additional unintended losses. In general, similar trends were observed for all microchannels and found to be consistent with the trends from the literature.

Loss coefficients were found to decrease with decreasing area ratio through both contractions and expansions. The minor loss coefficient data were found to be dependent on Reynolds number and the area ratio of the contraction/expansion at the bend. The

results suggest that the effect of the contraction/expansion was the dominant mechanism for minor losses in the 90° miter bend. The data presented in this study (friction factor, critical Reynolds number and minor loss coefficient) generally agree well with other reported data from the literature. There is no significant deviation from macroscale flow theory due to microscale effects. The results suggest that Stokes flow theory is applicable in describing flow behaviors of water flow in these rectangular xurographic microchannels.

6.2 Recommendations

Several recommendations to improve the quality of microchannels produced using xurography are presented in Chapter 4. A few other recommendations for future similar work involving xurographic microchannels include:

- Extend the range of the hydraulic diameter and aspect ratio of the microchannels. This can be accomplished using Kapton® tape with different thickness.
- Study the flow behavior in microchannel fabricated with tapes other than Kapton®.
- Due to cutting plotter imprecision, it is recommended that microchannel features be located a sufficient distance apart.
- Since a cutting plotter requires a change in cutting direction at abrupt features such as a 90° miter bend, the cut angle may deviate from the designed value. Characterization of the cut angle will be beneficial.
- Some adhesive droplets, uncut adhesive and other tripping elements may be present in the microchannel and interfere with the flow. Characterization of the

sizes of these defects in comparison to the channel dimensions may provide data useful in explaining the flow behaviors.

- Different materials, such as metals and plastics, could be used to cap the adhesive layers and polyimide film. These materials may bond differently during the curing process. An investigation of the material/adhesive bonding at different temperatures will provide useful information.
- The high uncertainty of the reported data, especially at low *Re*, can be improved by selecting pressure sensors that have a small pressure range.
- Thicker glass plates could be used to increase the clamping force on the microchannels, enabling higher *Re* flow. Data could then be obtained further into the turbulent flow regime.

The current study provides some general background and information regarding water flow in rectangular xurographic microchannels. In order to properly design microfluidic systems using xurography, further investigations of flow behaviors are needed in these microchannels. A few recommendations to extend the current study into areas of interests in microfluidic applications include:

- The hydrodynamic entrance length and re-establishment length after the bend or a contraction/expansion should be investigated for the flow in these xurographic microchannels.
- Data should be obtained for high *Re* flow in the turbulent regime for microchannels that have a high hydraulic diameter and low aspect ratio.
- Further investigations of minor losses in microchannels with curved bends and gradual contraction/expansion should be considered.

- The convective heat transfer in these xurographic microchannels within an appropriate temperature range (less than 100°C) should be examined. Counter-flow and cross-flow micro heat-exchangers using xurographic channels are good applications for this analysis.
- Investigation of microscale gas flow in various flow conditions and different channel geometries will be useful for some applications such as electronic cooling.
- Data on fluid mixing and interacting flow will be useful in designing micro-mixers, micro combustion reactors and more effective mixing of biological fluids.
- Investigation of two phase flows can also be conducted in these xurographic microchannels.

REFERENCES

[1] Zeng-Yuan Guo, Zhi-Xin Li, (2003), "Size Effect on Microscale Single-phase Flow and Heat Transfer," *International Journal of Heat and Mass Transfer* 46, pp. 149-159, 2003.

[2] Ian Papautsky, John Brazzle, Timothy Ameel, and A. Bruno Frazier, (1998), "Laminar Fluid Behavior in Microchannels using Micropolar Fluid Theory," *Sensor and Actuators* 17, pp. 101-108.

[3] Ki Band Lee and Liwei Lin, (2003), "Surface Micromachined Glass and Polysilicon Microchannels using MUMPs for BioMEMS Applications," *Sensor and Actuators* A. 111, pp. 44-50.

[4] Peng-FeiHoa, Feng He and Ke-Qin Zhu, (2005), "Flow Characteristics in a trapezoidal silicon microchannel," *Journal of Micromechanics and Microengineering*, 15, pp. 1362-1368.

[5] Vishal Singhal, Suresh V. Garimella, Jayathi Y. Murthy, (2004), "Low Reynolds Number Flow through Nozzle-Diffuser Elements in Valveless Micropumps," *Sensor and Actuators* A 113 (2004), pp. 226-235.

[6] MetinMuradoglu and Howard A. Stone, (2005), "Mixing in a Drop Moving in a Serpentine Channel: a Computational Study," *Physics of Fluid* 17, 073305 (2005).

[7] Byung-Ho Jo, Linda M. Van Lerberghe, Kathleen M. Motsegood, and David J. Beebe, (2000), "Three-Dimensional Micro-Channel Fabrication in Polydimethylsiloxane (PDMS) Elastomer," *Journal of Microelectromechanical Systems*, Vol. 1, No. 1, pp. 76-83, March 2000.

[8] C. Liu, Foundations of MEMS, Upper Saddle River, NJ: Pearson Prentice Hall, 2006.

[9] Bartholomeusz, D.A., Boutte, R.W., and Andrade, J.D., (2005), "Xurography: Rapid Prototyping of Microstructures using a Cutting Plotter," *Journal of Microelectromechanical Systems*, 14, pp. 1364-1374.

[10] Peng, X.F., Wang, B.X., (1994) "Liquid Flow and Heat Transfer in Microchannels with/without Phase Changes," *Proc. 10th International Heat Transfer Conference*, Brighton, UK, pp. 159-177.

[11] Yu, J., Li. Z., and Ma, C.F., (2006) "Experimental Study of Pressure Loss Due to Abrupt Expansion and Contraction in Mini-Channels," MIC-19, *International Heat Transfer Conference*, 13.

[12] Bing-Yang Cao, Min Chen, Zeng-Yuan Guo, (2006), "Effect of Surface Roughness on Gas Flow in Microchannels by Molecular Dynamics Simulation," *International of Engineering Sciences* 44, pp. 927-937, 2006.

[13] Y.D. Hu, C. Werner, D.Q. Li, (2003), " Influence of Three-Dimensional Roughness on Pressure-Driven Flow through Microchannels," *ASME Journal Fluid Engineering* 125, pp.871-879, 2003.

[14] J. Judy, D. Maynes, and B. W. Webb, (2002) "Characterization of Frictional Pressure Drop for Liquid Flows through Microchannels," *International Journal of Heat and Mass Transfer*, vol. 45, no. 17, pp. 3477-89, 2002.

[15] S, Kandlikar S. Garimella, D. Li, S. Colin, M.R. King, (2005), "Heat Transfer and Fluid Flow in Minichannels and Microchannels," 1st edition, Elsevier Science.

[16] S. V. Garimella and C. B. Sobhan, (2003), "Transport in Microchannels- A Critical Review," *Annual Review of Heat Transfer*, Vol 13.

[17] S. K. Roy and B. L. Avanik, (1996), "Very High Heat Flux Microchannel Heat Exchanger for Cooling of Semiconductor Laser Diode Arrays," *IEEE Trans. Components, Pack. Manuf. Technol. Part B: Advanced Packaging*, Vol. 19, pp. 444–451, 1996.

[18] Xiong, R. and Chung, J.N., (2006), "Flow Characteristics of Water in Straight and Serpentine Micro-Channels with Miter Bends," *Experimental Thermal and Fluid Science*, 31, pp. 805-812.

[19] Kolekar, R.D., (2009), "Fluid Flow Characteristics in Xurographic Microchannels," MS Thesis, Dept. of Mechanical Engineering, University of Utah, 2009.

[20] I. Papautsky, T. Ameel, A.B. Frazier, "A Review of Laminar Single Phase Flow in Microchannels," *Proceeding of 2001 ASME International Mechanical Engineering Congress and Exposition*, Nov. 11-16, 2001, NewYork, NY.

[21] Pfund, D., Rector, D., and Shekarriz, A., (2000), "Pressure Drop Measurements in a Microchannel," *AIChE Journal*, 46(8), pp. 1496-1507.

[22] W. Qu, Gh. M. Mala, D. Li, "Pressure Driven Water Flows in Trapezoidal Silicon Microchannel," *Int. J. Heat and Mass Transfer* 43, (2000), pp. 353-364.

[23] Costaschuk, D., Elsnab, J., Petersen, S., Klewicki, J.C., and Ameel. T., (2007), "Axial Static Pressure Measurements of Water Flow in a Rectangular Microchannel," *Experiments in Fluids*, 43, pp. 907-916.

[24] Kohl, M.J., Abdel-Khalik, S.I., Jeter, S.M., and Sadowski, D.L., (2004), "An Experimental Investigation of Microchannel Flow with Internal Pressure Measurements," *International Journal of Heat and Mass Transfer*, 48, pp. 1518-1533.

[25] Baviere, R., Ayela, F., Person, Le S., and Favre-Marinet, M., (2004) "An Experimental Study of Water Flow in Smooth and Rough Rectangular Micro-Channels," *2nd International Conference on Microchannels and Minichannels*, New York, NY, USA.

[26] B. Xu, K.T. Ooi, N.T. Wong, W.K. Choi, (2000), "Experimental Investigation of Flow Friction for Liquid Flow in Microchannels," *Int. Comm. Heat Transfer* 27, pp. 1165-1176, 2000.

[27] H.Y. Wu, P. Cheng, "Friction Factors in Smooth Trapezoidal Silicon Microchannels with Difference Aspect Rations," *Int. Journal of Heat mass Transfer* 46, (2003), pp. 2519-2525.

[28] Torgerson, D.E., 2010, "Microscale Loss Coefficients through Expansion and Contraction Xurographic Microchannels," MS Thesis, Dept. of Mechanical Engineering, University of Utah, 2010.

[29] Xiong, R., and Chung, J.N., 2008, "Effect of Miter Bend on Pressure Drop and Flow Structure in Microfluidic Channels," *International Journal of Heat and Mass Transfer*, 51, pp. 2914-2924.

[30] Maharudrayya, S., Jayanti, S., Deshpande, A.P., 2004, "Pressure Losses in Laminar Flow through Serpentine Channels in Fuel Cell Stacks," *Journal of Power Sources*, 138(1-2), pp. 1-13.

[31] Herwig, H., Schmandt, B., Uth, M.F., 2010, "Loss Coefficients in Laminar Flows: Indispensable for the Design of Micro Flow Systems," *8th International Conference on Nanochannels, Microchannels and Minichannels*, Montreal, Canada.

[32] D. Haller, P. Woias, and N. Kockmann, "Simulation and Experimental Investigation of Pressure Loss and Heat Transfer in Microchannel Networks Containing Bends and T-junctions," *International Journal of Heat and MassTransfer*, vol. 52, no. 11-12, pp. 2678-2689, 2009.

[33] S. Y. K. Lee, M. Wong, and Y. Zohar, "Gas Flow in Microchannel with Bends," *Journal of Micromechanics and Microengineering*, Vol 11, no. 6, pp. 365-644.

[34] Zho, L., Jian, Y.U., and ChongFang, M.A., 2008, "Characteristics of Pressure Drop for Single-phase and Two-phase Flow across Sudden Contraction in Microtubes," *Science in China Series E: Technological Science*, 51(2), pp.162-169.

[35] Abdellal, F.F., Hahn, G., Ghiaasiaan, S.M., Abdel-Khalik, S.I., Jeter, S.S., Yodo, M., and Sadowski, D.L., 2004, "Pressure Drop Caused by Abrupt Flow Area Changes in Small Channels," *Exp. Thermal and Fluid Sciences*, 29, pp. 71-78.

[36] Chalfi, T., 2007, "Pressure Loss Associated with Flow Area Change in Micro-Channels," MS Thesis, Dept. of Mechanical Engineering, Georgia Institute of Technology.

[37] Wiginton, C.L. and Dalton, C., 1970 "Incompressible Laminar Flow in the Entrance Region of a Rectangular Duct" *Transactions of the ASME Series E, Journal of Applied Mechanics,* 37, pp. 854-856.

[38] Fox, R.W., and McDonald, A.T., 1998, "Introduction to Fluid Mechanics," 5th ed., Wiley, New York.

[39] Weast, R.C., ed., 1988, CRC Handbook of Chemistry and Physics, 1st Student Ed., Boca Raton, FL, CRC Press.

[40] Shah, R.K., and London, A.L. 1978, "Laminar Flow Forced Convection in Ducts: a Sourcebook for Compact Heat Exchanger Analytical Data," New York, Academic Press.

[41] Torgerson, D., Kolekar, R., Gale, B., and Ameel, T., 2010, "Minor Losses in Rectangular Xurographic Microchannels," *Proc. ASME International Congress and Exhibition*, Paper IMECE 2010-39401, Vancouver, British Columbia, Canada.

[42] Smith, B.L., 2004 "Pressure Recovery in a Radiused Sudden Expansion," *Experiments in Fluids*, 36, pp. 901-907.

[43] Moffat, R.J., 1998, "Describing the Uncertainties in Experimental Results," *Experimental Thermal and Fluid Science*, 1, pp.3–17.

[44] Makiranta, J. Kallio, P. Lekkala, J. "A Novel Modeling Method of Surface Roughness in a Mircofluidc Channel," SIMS2005, *Scandinavian Conference on Silumation and Modeling*, 2005.

[45] H.Y Wu, P. Cheng, "An Experimental Study of Convective Heat Transfer in Silicon Microchannels with Different Surface Conditions," *International Journal of Heat and Mass Transfer*, Vol. 46, pp. 2547-2556, 2003.

[46] S.G. Kandlikar, S. Joshi, and S. Tian, "Effects of Surface Roughness on Heat Transfer and Fluid Flow Characteristics at Low Reynolds numbers in Small Diameter Tubes," *Heat Transfer Engineering*, Vol. 24, No. 3, pp. 3-16, 2003.

[47] S.G. Kandlikar, "Roughness Effects at Mircoscale –Reassessing Nikuradsels Experiments on Liquid Lfow in Rough Tubes," *Bulletin of the Polish Academy of Science Technical Sciences*, Vol. 53, No. 4, pp. 343-349, 2005.